INL/EXT-21-64176

Demonstrate Capability of NEAMS Tools to Generate Reactor Kinetics Parameters for Pebble-Bed HTGRs Transient Modeling

August 2021

HTGR Application Drivers - M2MS-21IN0801042

Ryan Stewart[1], David Reger[2], and Paolo Balestra[1]

[1]*Idaho National Laboratory*
[2]*Pennsylvania State University*

Idaho National Laboratory

INL is a U.S. Department of Energy National Laboratory operated by Battelle Energy Alliance, LLC

INL/EXT-21-64176

Demonstrate Capability of NEAMS Tools to Generate Reactor Kinetics Parameters for Pebble-Bed HTGRs Transient Modeling

HTGR Application Drivers - M2MS-21IN0801042

Ryan Stewart[1], David Reger[2], and Paolo Balestra[1]

[1]**Idaho National Laboratory**
[2]**Pennsylvania State University**

August 2021

Idaho National Laboratory
Idaho Falls, Idaho 83415

http://www.inl.gov

Prepared for the
U.S. Department of Energy
Office of Nuclear Energy
Under DOE Idaho Operations Office
Contract DE-AC07-05ID14517

Page intentionally left blank

ABSTRACT

The system analysis of anticipated operating occurrences and design basis accident for pebble-bed reactor systems requires knowledge of the neutron kinetic parameters. These parameters take into account various types of feedback from the pebble-bed core and are typically integrated into system analysis tools such as the System Analysis Module (SAM) in the Nuclear Energy Advanced Modeling and Simulation (NEAMS) tool package. These parameters are typically generated by a higher fidelity full-core coupled neutronics/thermal fluids analysis, such as using Griffin and Pronghorn, in 2D or 3D. The delayed neutron fractions (beta) and the neutron lifetimes (lambda) are typically generated by applying the adjoint solution of the neutron flux. Temperature reactivity coefficients are the most important feedback for all anticipated operating occurrences and design basis accident, then depending on the transient other effects might be important as rector control system worth, s-curves, and Xenon generation. This work package will establish a methodology and process for calculating the reactor kinetics parameters for high-temperature gas-cooled reactor and provide them in a suitable form for system level analyses of typical anticipated operating occurrences and design basis accident.

Page intentionally left blank

CONTENTS

FIGURES

TABLES

ACRONYMS

BC	boundary condition
CFD	computational fluid dynamics
DF	discontinuity factor
HTGR	high-temperature gas-cooled reactor
IQS	improved quasi static
NEAMS	Nuclear Energy Advanced Modeling and Simulation
NK	neutron kinetic
PBR	pebble-bed reactor
PKE	point kinetic equations
RCS	rector control system
RSS	reserve shutdown system
SAM	System Analysis Module
SPH	super homogenization
TH	thermal hydraulic
TRISO	TRi-structural ISOtropic

Page intentionally left blank

1. CODES DESCRIPTION

Griffin is a MOOSE-based [3] reactor physics code that combines the capabilities of Rattlesnake [4], Proteus [5], and MC2-3 [6]. The transient, multiphysics capabilities of Rattlesnake are discussed in length in [7]. Griffin supports lower-order operator such as diffusion with homogenization equivalence via super homogenization (SPH) factors and discontinuity factors (DFs) or PKE that is ideal for reducing costs of simulating HTGR transients. Griffin relies on nuclear data generated by some other code suite; for this work, the SERPENT Monte Carlo code is used [8]. Two codes within Griffin will also be used: ISOXML and the Point Kinetics Equations (PKE) module. ISOXML provides support for converting generated cross sections into an XML format for Griffin to use [9]. The PKE module solves the point kinetics equations and can be used to determine reactor power without the need for a detailed neutronics solve.

Pronghorn is a MOOSE-based intermediate-fidelity coarse-mesh thermal-hydraulics tool that is less expensive than traditional computational fluid dynamics (CFD) software, but it offers more accuracy for inherently multidimensional flow fields [10–12]. It solves the multidimensional, compressible, and incompressible Euler equations (leveraging the Navier-Stokes MOOSE module and incompressible flow features [13]) for porous and non-porous flow configurations. In contrast to CFD, Pronghorn does not resolve small flow features (e.g., boundary layers). Instead, it captures their effect on the average-flow variables using correlations. While this is similar to system codes, Pronghorn is distinctly able to account for multidimensional effects which are crucial in pebble-bed reactors (PBRs) concepts. Griffin can readily integrate with Pronghorn via the MOOSE framework, allowing for a fully coupled system (i.e., all variables are solved within a single nonlinear system of equations).

SERPENT is a full 3D Monte Carlo neutronics code. Serpent was selected for two reasons: first, as reference solution to verify the Griffin model and second, Serpent can generate homogenized cross sections treating the double heterogeneity of the TRi-structural ISOtropic (TRISO)/pebble fuel system (capability currently under development in Griffin). Reactor geometries can be set by creating using Boolean logic to combine various geometric cells until a representative core is created. Each cell is then filled with a material to represent the associated isotopics. For this work, Serpent creates a separate HTGR model to generate equivalent cross sections for various regions

and provides a comparison for some PKE parameters.

2. METHODOLOGY DESCRIPTION

The process of generating reactor kinetics parameters for a HTGR is split into multiple steps. The general flow can be seen in Figure 1 and is outlined in Section 2.2. Along with this, Section 2.1 develops the mathematical basis for generating PKE parameters in Griffin as derived from [4]. Steps are highlighted here and described in further detail in the report:

1. Generate Serpent, Griffin, and Pronghorn models, ensuring model compatibility (Section 2.2.1)
2. Generate macroscopic cross sections using Serpent and convert cross sections to a format Griffin can interpret (Section 2.2.2)
3. *Optional*: Calculate SPH factors to correct the cross sections if low-order diffusion solvers are used (Section 2.2.3)
4. Perform steady-state Griffin calculation (Section 2.2.3)
5. Perform null-transient using improved quasi static (IQS) in Griffin to ensure stable steady-state solution and to generate PKE parameters (Section 2.2.4)
6. *Optional*: Generate global/local reactivity coefficients using IQS in Griffin (Section 2.2.5)
7. *Optional*: Repeat process with additional fidelity or characteristics until a realistic model is achieved (Section 3).

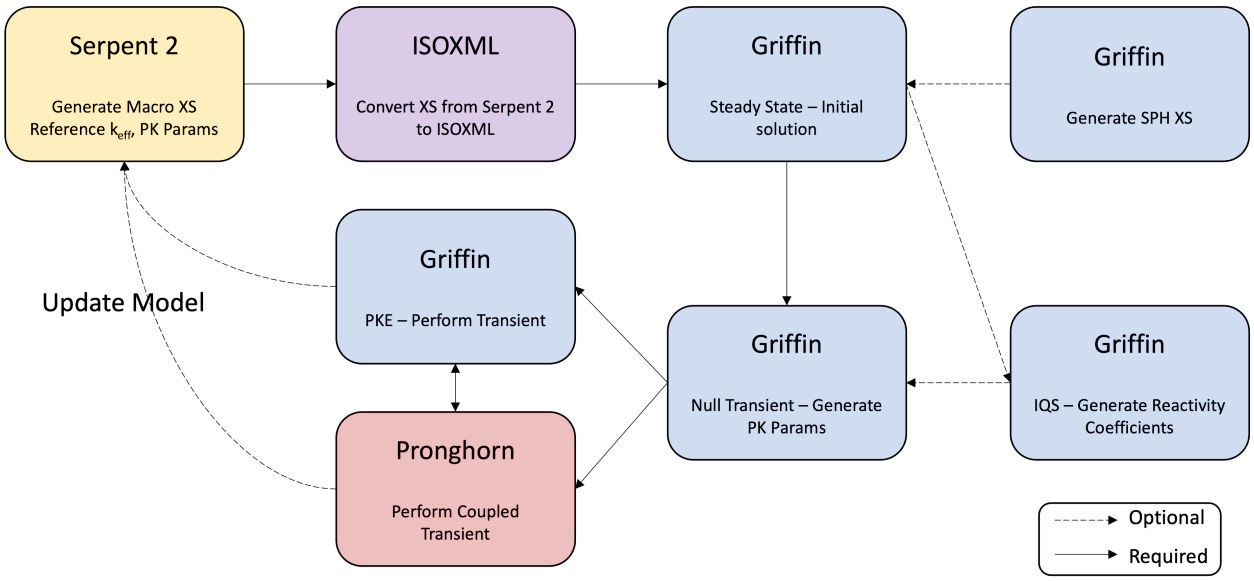

Figure 1: General flow for generating and using PKE parameters in Griffin.

2.1 Background: Improved Quasi Static (IQS) Theory

Griffin uses the IQS methodology for generating time integrated spatial kinetics parameters. The basis of IQS involves leveraging the ability to factor the flux into a scalar time-dependent amplitude and a shape function. Splitting the flux into two components is allowed due to the fact that the time dependence of the shape function is typically weaker than the flux itself. To provide some context for the use of IQS, we begin by writing out the neutron transport equation (given in its abstract weak form for a transient problem):

$$\mathbb{T}\left(\mathbf{\Psi}^*, \frac{\partial}{\partial t}\left(\frac{\mathbf{\Psi}}{\mathbf{v}}\right)\right) = \mathbb{F}(\mathbf{\Psi}^*, \mathbf{\Psi}) - \mathbb{L}(\mathbf{\Psi}^*, \mathbf{\Psi}) + \mathbb{S}(\mathbf{\Psi}^*, \mathbf{\Psi}) - \sum_{i=1}^{I} \mathbb{F}_{\mathrm{d},i}(\mathbf{\Psi}^*, \mathbf{\Psi}) + \sum_{i=1}^{I} \mathbb{S}_{\mathrm{d},i}(\mathbf{\Psi}^*, C_i), \quad (1)$$

$$\frac{d}{dt}(C_i^*, C_i)_{\mathcal{D}} = (C_i^*, \mathbb{P}_i \mathbf{\Phi})_{\mathcal{D}} - (C_i^*, \lambda_i C_i)_{\mathcal{D}}, \quad i = 1, \cdots, I, \quad (2)$$

where $\mathbb{T}$, $\mathbb{F}$, $\mathbb{L}$, $\mathbb{S}$, $\mathbb{F}_{\mathrm{d},i}$, $\mathbb{S}_{\mathrm{d},i}$ are the time, fission, loss due to streaming and collision, scattering, delayed fission, and delayed source kernels of the flux $\mathbf{\Psi}$. We introduce the factorized flux in Equation 3, where n is the amplitude and ψ is the shape.

$$\mathbf{\Psi}(\vec{x}, \vec{\Omega}, t) = n(t)\psi(\vec{x}, \vec{\Omega}, t), \quad (3)$$

Along with this, we introduce the weighing function $\mathbf{\Psi}^*$ as the adjoint flux. The adjoint flux provides information about the importance of neutrons in a specified area. After a short derivation (described in detail in [4]), we obtain the PKE (Equations 4 and 5) with the PKE parameters (Equations 6–11).

$$\frac{dn}{dt} = \frac{\rho - \beta_{\mathrm{eff}}}{\Lambda} n + \sum_{i=1}^{I} \lambda_i \xi_i, \quad (4)$$

$$\frac{d\xi_i}{dt} = \frac{\beta_{\mathrm{eff},i}}{\Lambda} n - \lambda_i \xi_i, i = 1, \cdots, I. \quad (5)$$

$$\rho = \frac{(\mathbb{F} - \mathbb{L} - \mathbb{S})(\boldsymbol{\psi}^*, \boldsymbol{\Psi}) + \mathbb{T}_t'(\boldsymbol{\psi}^*, \frac{\boldsymbol{\Psi}}{\mathbf{v}})}{\mathbb{F}(\boldsymbol{\psi}^*, \boldsymbol{\Psi})}, \tag{6}$$

$$\beta_{\text{eff},i} = \frac{\mathbb{F}_{\text{d},i}(\boldsymbol{\psi}^*, \boldsymbol{\Psi})}{\mathbb{F}(\boldsymbol{\psi}^*, \boldsymbol{\Psi})}, \tag{7}$$

$$\Lambda = \frac{\mathbb{T}(\boldsymbol{\psi}^*, \frac{\boldsymbol{\Psi}}{\mathbf{v}})}{\mathbb{F}(\boldsymbol{\psi}^*, \boldsymbol{\Psi})}, \tag{8}$$

$$\lambda_i = \frac{(C_i^*, \lambda_i C_i)_{\mathcal{D}}}{(C_i^*, C_i)_{\mathcal{D}}}, \tag{9}$$

$$\beta_{\text{eff}} \equiv \sum_{i=1}^{I} \beta_{\text{eff},i}, \tag{10}$$

$$\xi_i = \frac{(C_i^*, C_i)}{\mathbb{T}(\boldsymbol{\psi}^*, \frac{\boldsymbol{\psi}}{\mathbf{v}})}, i = 1, \cdots, I. \tag{11}$$

Where IQS is used in Griffin to evaluate $\beta_{\text{eff},i}$, Λ, λ_i, β_{eff}, and ξ_i. These values can be stored and utilized in the PKE equations (Equations 4 and 5). If a known reactivity (ρ) is added, this can be used to determine the change in neutron amplitude. For this work, the change in reactivity will be associated with a thermal feedback (determined using Pronghorn), where reactivity coefficients will be generated to determine the change in reactivity per unit temperature.

The thermal feedback is broken in to three reactivity coefficients: (1) fuel, (2) moderator, and (3) reflector. The temperature reactivity coefficient for each is given by Equation 12, where 'coeff' refers to either fuel, moderator, or reflector. The units for Equation 12 are given in terms of pcm/K.

$$\rho_{T,coeff} = \frac{\Delta\rho}{\Delta T} \tag{12}$$

where (note that $\Delta\rho$ is described in terms of per-cent milli [pcm]) $\Delta\rho$ can be described in terms of k_{eff} (k_1, k_2) values or reactivity (ρ).

$$\Delta\rho = \frac{k_2 - k_1}{k_2 * k_1} * 10^5. \tag{13}$$

$$\Delta\rho = (\rho_2 - \rho_1) * 10^5. \tag{14}$$

2.2 Procedure for Generating PKE Parameters

2.2.1 Simplified Core Model

To outline the procedure required for generating PKE parameters, a simplified HTGR model was used. The simplified design for the HTGR comprised of a bed of fuel pebbles and was surrounded radially and axially by a graphite reflector. No cavity was modeled in the simplified core model as it has a low-neutronic importance and requires increased computational resources to accurately calculate macroscopic cross sections. The pebble-bed region of the HTGR had an axial height of 8.93 m with a radius of 1.20 m [1]. Surrounding the pebble-bed region was a 0.5 m axial reflector and 1.0 m radial reflector. Figures 2 and 3 show the core layout of the HTGR. Control/safety rods, riser channels, and the fuel chute are not modeled in the simplified core design. The simplified core design was meant to provide a simple, yet representative, HTGR model which will only be used for showcasing the methodology for generating PKE parameters.

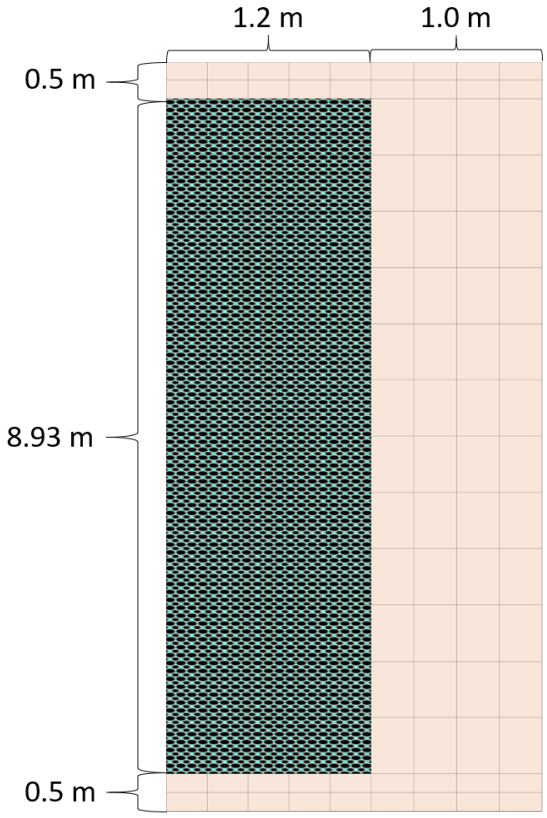

Figure 2: Axial layout for simplified HTGR core model.

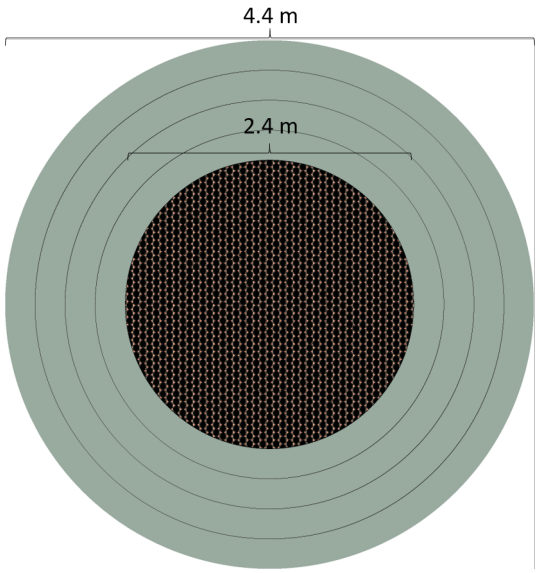

Figure 3: Radial Layout for Simplified HTGR Core Model.

2.2.2 Generation of Macroscopic Cross Sections

The Serpent model was used to generate macroscopic cross sections for this HTGR. The Serpent geometry was partitioned into multiple regions (called universes in Serpent), which allowed for the creation of a macroscopic cross section in each region. For the simplified model, the fuel region was split into 60 regions and the reflector into 84 regions. Utilizing a large number of regions for both the fuel and reflector regions allows for accurate spatial cross-section generation.

Cross sections were generated at three different state points for the temperature of the fuel: 600 K, 900 K, and 1200 K. For each temperature state point, a separate Serpent execution was required. Serpent also generated the k_{eff} and PKE parameters; this allowed for a comparison between the Griffin generated PKE parameters. The k_{eff} was also used to generate SPH corrected cross-section generation.

The macroscopic cross sections from Serpent were then converted to an XML file format using the Griffin module ISOXML [9]. The macroscopic cross sections were a four energy group structure based off [14]. Once the cross-section sets were generated, the XML files could be used by both the steady state and transient models. A 2D Griffin model leveraged an RZ coordinate system with axial and radial dimensions that were identical with the Serpent model. This allowed

the cross sections generated by ISOXML to be used in each respective region in Griffin. A vacuum boundary condition (BC) was applied to both axial edges and the edge of the radial reflector region. A reflective BC was applied to the inner edge of the core. The Griffin model utilized diffusion as the transport solver.

2.2.3 Griffin Steady-State Initial Solution and SPH Procedure

Upon gathering appropriate cross sections for the simplified model, an initial check is made between Griffin and Serpents steady-state solution. Along with this, SPH-factors were generated to preserve the flux for the low-order diffusion solve. The resulting k_{eff} can be seen in Table 1; Serpent uncertainty was given by (_). The cross sections generated using this method did not exactly reproduce k_{eff}, and was off by approximately 350 pcm.

	600 K	900 K	1200 K
Serpent	1.37959 (1.4E-05)	1.35652 (1.4E-05)	1.33673 (1.4E-05)
Griffin	1.386706	1.362973	1.342726
Diff. (pcm)	372	349	344

Table 1: Griffin steady-state analysis comparison.

To reproduce the results obtained by Serpent, the cross sections were corrected using SPH factors. This was done by using the equivalence block in Griffin and iterating over each of the state points to generate an updated cross-section set. For regions that were far away from the core, it was necessary to neglect the SPH factors. This was due to the fact that the flux in areas of low importance usually had a much higher level of uncertainty, which can cause the SPH calculations to not converge. We found calculating SPH-factors for the fuel region and adjacent reflector region was enough to reproduce flux values and global neutronics data found in Serpent. Table 2 shows using SPH-corrected cross sections reproduced the Serpent results exactly.

	600 K	900 K	1200 K
Serpent	1.37959 (1.4E-05)	1.35652 (1.4E-05)	1.33673 (1.4E-05)
Griffin	1.379590	1.356520	1.336730
Diff. (pcm)	0	0	0

Table 2: Griffin steady-state analysis comparison with SPH corrected cross sections.

2.2.4 Null Transient and PKE Parameter Generation

A null transient using the IQS method was used to generate the PKE parameters. The null transient (i.e., a transient with no change to the system over time) was performed to ensure the steady-state solution was stable. A stable solution (i.e., a solution where the neutron population does not vary when no excess reactivity is present) was required before running a transient solution. Only the SPH-corrected cross-section sets are examined for the null transient analysis. The PKE parameters are compared with Serpent.

A transient analysis could be run in two ways: a multi-app system or performing the steady-state and transient problem separately. For this analysis, the former approach was used. This allowed the steady-state problem to be executed where all outputs (such as flux, transport solution, etc.) were written to binary files. The transient analysis could then read the binary files.

Table 3 shows the values for betas, lambdas, and the mean generation time for SPH-corrected parameters. There was good agreement for betas and lambdas obtained by Serpent; however, results for the mean generation time were off and required further investigation (see Appendix A). Preliminary analysis shows the difference in mean generation time does not affect the overall shape of transients using PKE parameters but does affect the amplitude. Further investigation is ongoing as to why this difference occurs.

	Beta-0	Beta-1	Beta-2	Beta-3	Beta-4	Beta-5
Serpent	2.323E-04	1.199E-03	1.145E-03	2.568E-03	1.059E-03	4.431E-04
Griffin	2.321E-04	1.199E-03	1.145E-03	2.568E-03	1.059E-03	4.430E-04
Diff. (%)	0.092	0.018	0.024	0.026	0.031	0.030
	Lambda-0	Lambda-1	Lambda-2	Lambda-3	Lambda-4	Lambda-5
Serpent	1.334E-02	3.273E-02	1.208E-01	3.029E-01	8.500E-01	2.855E+00
Griffin	1.334E-02	3.273E-02	1.208E-01	3.029E-01	8.500E-01	2.855E+00
Diff. (%)	0.000	0.000	0.000	0.000	0.000	0.000
	Mean Gen. Time					
Serpent	4.995E-04					
Griffin	8.745E-04					
Diff (%)	75.075					

Table 3: Comparison of average PKE parameters at 900 K using SPH-corrected values for the simplified core mode.

2.2.5 Generation of Global/Local Reactivity Coefficients

For the simplified model, a single reactivity coefficient for the fuel temperature was examined. The fuel temperature coefficient was calculated as a global reactivity coefficient and distributed local reactivity coefficients.

To calculate the global fuel reactivity coefficient, the IQS solver was used to perform a transient where the temperature of the fuel was adjusted by 1 K. This transient tracked the reactivity insertion due to the change in temperature, where the reactivities at 900 and 899 K are used to generate $\Delta\rho$.

To calculate the local reactivity coefficients for the fuel temperature, each element (1/4 of a block) in the core (576 elements total) were adjusted by 1 K independently. This meant that 576 separate Griffin cases were executed. The resulting fuel coefficients were then compared. Table 4 shows the reactivity for the transient for the full core and element-wise analysis, where we find a difference of less than 0.01%.

	Reactivity	Reactivity Coefficient (pcm/K)
Full Core	2.92491106e-04	5.84982
Element-Wise	2.92498330e-04	5.84997
Difference (%)	-0.0025	-0.0025

Table 4: Comparison of global and local reactivity coefficients for the simplified model.

The method to calculate global and local reactivity coefficients for the simplified model only examined the fuel. This provided a methodology for determining these coefficients and could easily be applied to additional feedback coefficients such as the moderator or reflector.

2.3 Neutronics Model

This work generated cross sections using the Monte-Carlo neutron transport code Serpent [8], and as such, the HTGR was built in Serpent separately from Griffin. It was imperative the geometry present in Serpent matched the geometry present in Griffin/Pronghorn as the cross section generated were geometry dependent. Serpent used a 3D model, where Griffin/Pronghorn used a 2D RZ geometry; as such, it was important to ensure appropriate regions were created which can be translated from 3D to 2D RZ. The neutron kinetic (NK) model was based on open-source documentation [1, 15].

We begin with a description of the fuel pebbles used in HTGR core. Figure 4 shows an example of the fuel pebble with TRISO fuel randomly distributed throughout. The geometry of the fuel pebble and kernel are described in Table 5. Each fuel pebble contained approximately 7 grams of uranium. Fuel kernels were enriched to 15.56%, and the isotopics can be seen in Table 6.

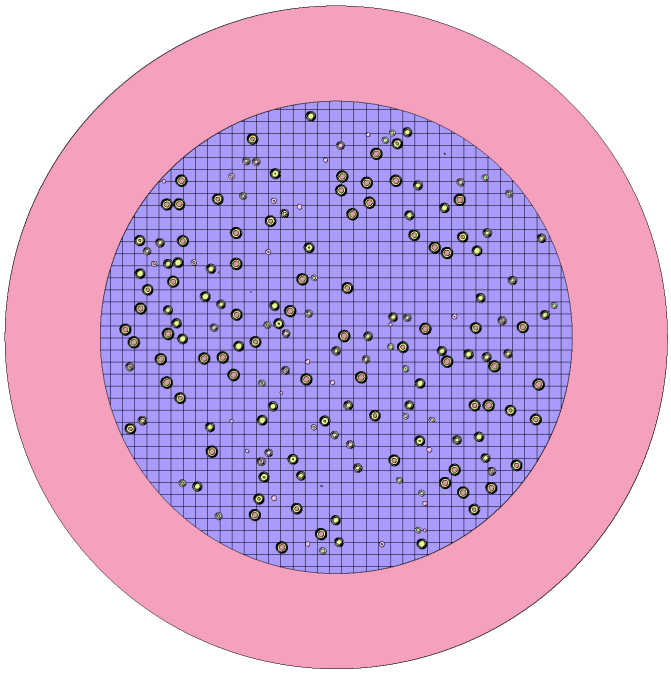

Figure 4: Fuel pebble with randomly distributed TRISO kernels.

Fuel Pebble		Fuel Kernel	
Outer Radius (mm)	30.0	PyC Outer Radius (mm)	0.4275
Carbon Matrix Outer Radius (cm)	25.0	SiC Outer Radius (mm)	0.3875
		PyC Outer Radius (mm)	0.3525
		Buffer Outer Radius (mm)	0.3125
		UCO Outer Radius (mm)	0.2125

Table 5: Fuel pebble and kernel geometric data [1].

For the realistic NK core model additional features including the cavity, control/safety rods, riser channels, fuel chute, outlet channel, and outlet plenum were modeled. The pebble-bed region of the HTGR maintained the axial/radial dimensions; however, the fuel chute extended an extra 1.26 m below the core [1]. Above the core was a 0.55 m cavity filled with helium. Control/safety rods (and their associated tube) and riser channels were introduced to the radial reflector. Figure 5 shows the core layout of the HTGRs. The control/safety rods were located adjacent to the core,

Isotope	Atomic Density
U-234	$7.87E^{-}5$
U-235	$3.91E^{-}3$
U-236	$8.14E^{-}6$
U-238	$2.10E^{-}2$
O-16	$3.40E^{-}2$
C	$8.13E^{-}3$
Total	$6.71E^{-}2$

Table 6: Fuel kernel isotopics [2].

where 18 bore holes which comprise the control rods (seen in violet) and safety rods (not shown) were filled with helium when the control/safety rods are not inserted. Control rods were placed approximately 75 cm into the fuel. Each control/safety bore hole had a 6.5 cm radius and extended the length of the core region. Past the control rods, there are 18 coolant risers (each with a 9.0 cm radius) which extend the length of the core and culminated in a helium void at the same axial height as the cavity region. The outlet channel and outlet plenum region were comprised of graphite with a lower density to account for flow channels in these regions.

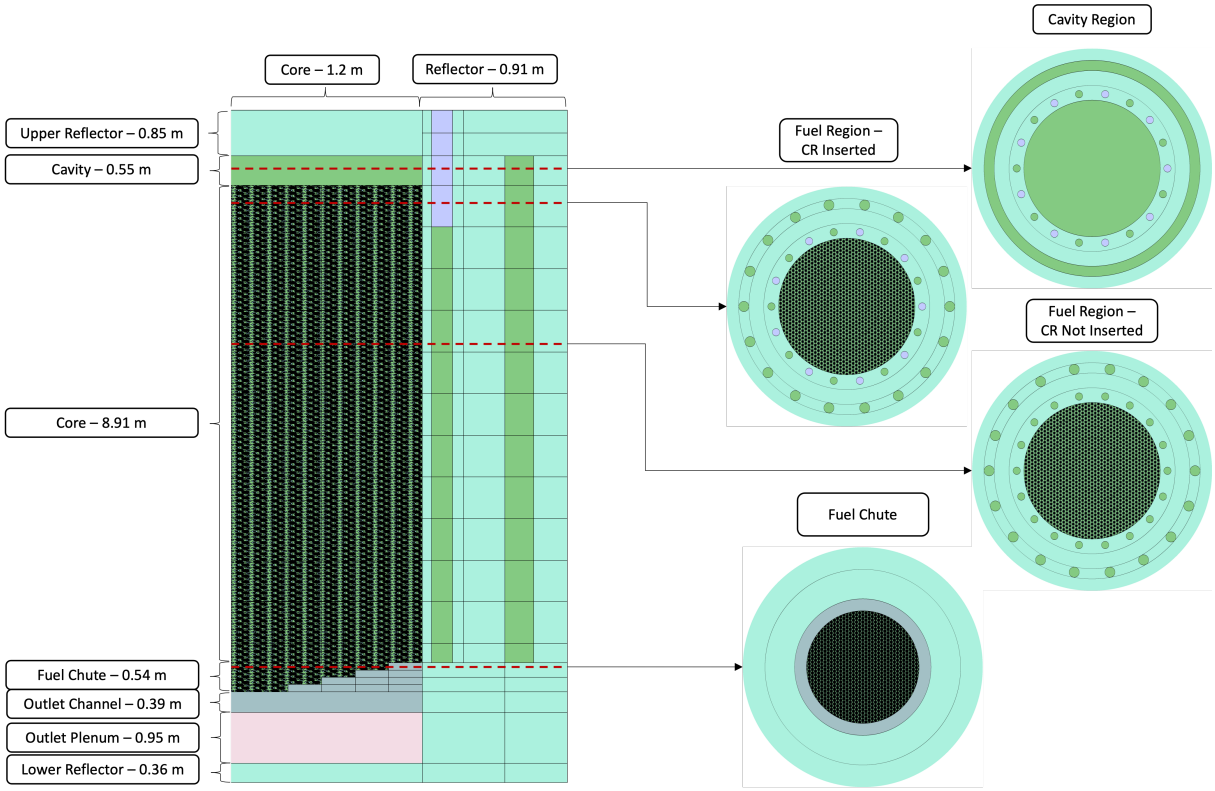

Figure 5: Layout for the realistic HTGR core model.

2.4 Thermal Hydraulic Model

A thermal hydraulic (TH) model of the HTGR was developed to provide fluid, fuel, moderator, and reflector temperatures for use in determining temperature feedback in the NK models. Similarly to the NK model, the TH model was created based on the available literature data to model a typical PBR that could be deployed in the coming years. This model was comprised of a bed of fuel pebbles surrounded by a graphite moderator. The core inlet, riser channel, top cavity, and outlet plenum were included in the TH model. Additionally, the core barrel and reactor pressure vessel were included in order to account for their effects on heat removal from the system. Geometric data for this system was roughly estimated using publicly available figures and models, and the significant feature dimensions can be found in Table 7. The resulting model can be seen in Figure 6. Dimensions were generated by using publicly available dimensions, such as the core radius, to determine a conversion factor between image pixels and feature length in meters.

The porosity values for the regions of the system are recorded in Table 8. The porosity value

Feature	Dimension
Core Radius	1.2 m
Reflector between Core and Riser Width	0.52 m
Riser Width	0.18 m
Outer Reflector Width	0.21 m
Ref/Barrel Gap	0.04 m
Barrel Thickness	0.04 m
Barrel/RPV Gap	0.08 m
RPV Thickness	0.09 m
Bottom Reflector Height	0.589 m
Core Height	8.93 m
Core Inlet Height	0.36 m
Riser Height	8.57 m
Top Gap Height	0.55 m
Top Reflector Height	0.85 m

Table 7: Dimensions of significant geometric features included in the TH model.

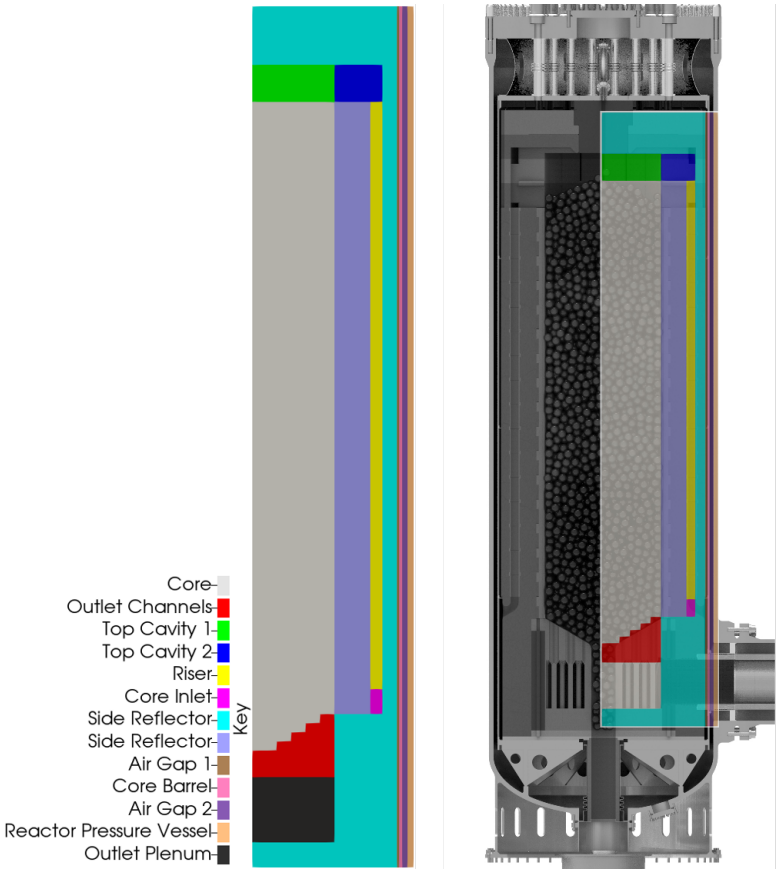

Figure 6: TH model (left) and TH model overlayed over the Xe-100 opensource figure used to determine system dimensions (right).

of the pebble bed was determined by dividing the quoted volume of the core by the total volume of the 223,000 pebbles to determine the packing fraction and subtracting this fraction from 1.

$$\epsilon_{bed} = 1 - \frac{\text{Volume of pebbles}}{\text{Volume of core vessel}} = 1 - \frac{(223,000)(\frac{4\pi}{3})(0.03^3)}{41.27} = 0.39 \tag{15}$$

To determine the porosity in other regions of the core, a few assumptions were made. Risers in HTGRs are typically formed by drilling holes through the graphite blocks of the reflector in order to form a channel for the helium to pass through.

In [1], it is indicated a reactor of this size has 18 holes for the rector control system (RCS) and reserve shutdown system (RSS). Making the assumption the number of riser holes is the same of the RCS and RSS as indicated in several pictures of different designs, there would be 18 riser channels. The porosity was calculated by computing the ratio of areas between the 18 riser channels and the circular shell in which they lie.

$$\epsilon_{riser} = \frac{\text{Area of riser channels}}{\text{Total Shell Area}} = \frac{18\pi(0.09)^2}{\pi(1.9^2 - 1.72^2)} = 0.22 \tag{16}$$

Information for the outlet channels was determined using the same image method used for the rest of the geometric features. For both the outlet channels and outlet plenum, only half of the system was used to determine the porosity, as the pebble exit chute was blocking the view in the center, preventing any information on these features from being determined in the middle of the system. It was determined from the images in a section of the outlet, there were roughly 30 channels of 0.0077 m width across 0.91 m of total width. Since it is only possible to get the dimensions in the orientation pictured, a 1D approximation of the porosity was necessary.

$$\epsilon_{OutletChannels} = \frac{\text{Total Width of Channels}}{\text{Total Width of Region}} = \frac{30(0.0077)}{0.9163} = 0.25 \tag{17}$$

The porosity of the outlet plenum was determined in the same manner as the outlet channels, also with the 1D approximation. The five channels in the image were determined to each have a width of 0.0616 m, and they spanned across a total width of 0.91 m.

Region	Porosity
Core	0.39
Riser	0.22
Outlet Channels	0.25
Outlet Plenum	0.34
Voids	1.0

Table 8: Porosity values assigned to the porous regions of the system.

3. RESULTS AND ANALYSIS

The results presented in this section utilize the NK and TH models presented in Sections 2.3 and 2.4. The same procedure outlined in Section 2.2 was followed to generate each of the components required for full transient analysis. Intermediate steps are not included in this section, and only results are given.

3.1 Global and Local PKE Parameters

Global and local PKE parameters were generated twice: once for a core with a constant 900 K temperature profile and a second time for a core with temperature profile generated from Pronghorn. The PKE parameters were calculated following the procedure outlined in Section 2.2.4. Table 9 shows the PKE parameters for both Serpent and Griffin. There is good agreement found for both the betas and lambdas; however, there is still a significant difference in the mean generation time.

Table 10 shows the reactivity coefficients for each of three regions, along with the total reactivity coefficient. The results obtained from Griffin do not exactly match the Serpent results. This is due to the fact Griffin scales the transport equation by k_{eff} to obtain a stable configuration during the transient simulation (in this case is high due to the fresh fuel), resulting in a larger reactivity coefficient. Dividing the reactivity coefficients from Griffin by the steady state k_{eff} provides a close approximation with Serpent. The remaining difference is likely due to the fact the Serpent coefficients were calculated using a 300 K reactivity excursion (using the k_{eff} of two temperature tabulation points) that provides an average value of the coefficients in that interval (reactivity coefficients has a temperature dependence). Griffin calculates the reactivity coefficients using information (flux and adjoint flux) at the state point.

	Beta-0	Beta-1	Beta-2	Beta-3	Beta-4	Beta-5
Serpent	2.319E-04	1.202E-03	1.143E-03	2.576E-03	1.066E-03	4.465E-04
Griffin	2.344E-04	1.210E-03	1.150E-03	2.588E-03	1.070E-03	4.486E-04
Diff. (%)	-1.052	-0.675	-0.691	-0.469	-0.465	-0.469
	Lambda-0	Lambda-1	Lambda-2	Lambda-3	Lambda-4	Lambda-5
Serpent	1.334E-02	3.273E-02	1.208E-01	3.029E-01	8.501E-01	2.855E+00
Griffin	1.334E-02	3.273E-02	1.208E-01	3.029E-01	8.501E-01	2.855E+00
Diff. (%)	-0.001	0.000	0.000	0.000	0.001	-0.003
	Mean Gen. Time					
Serpent	5.116E-04					
Griffin	6.519E-04					
Diff (%)	27.424					

Table 9: Comparison of PKE parameters at 900 K using SPH-corrected values for the realistic core model.

	Griffin	Griffin (k_{eff} Scaled)	Serpent
Fuel	-4.53900	-3.41090	-3.3084
Moderator	-3.82551	-2.87658	-2.7281
Reflector	2.19416	1.64988	1.6285
Total	-6.1704	-4.6398	-4.4080

Table 10: Temperature reactivity coefficients (pcm/K) for the realistic HTGR model.

Upon calculating the global reactivity coefficient using both Griffin and Serpent, the local reactivity coefficients were calculated. Figures 7–9 show the local reactivity coefficients for the fuel, moderator, and reflector. Along with this, Table 11 shows the global fuel, moderator, reflector, and total reactivity coefficients calculated using using the local and the global reactivity. We find the local reactivity coefficients perform very well when used to calculated global reactivity coefficients.

	Fuel	Moderator	Reflector	Total
Full Core	-4.53900	-3.82551	2.19416	-6.17069
Element-Wise	-4.53953	-3.82596	2.19403	-6.17146
Difference (%)	-4.34E-3	-1.17E-2	5.88E-3	-1.25E-2

Table 11: Comparison of global and local reactivity coefficients for the realistic model.

Local reactivity coefficients were initially generated using the steady-state core, where the temperature was constant (900 K) across the core. We also determined the local reactivity coefficients using a more realistic temperature profile from the coupled Pronghorn-Griffin case. This provided a set of local reactivity coefficients which would represent a realistic HTGR.

Figures 7–9 show the steady-state and coupled local reactivity coefficients, along with the difference between the two coefficients. The relative difference is not presented as many of the coefficients were extremely small and often caused large relative differences that were insignificant. For the fuel coefficients, the negative feedback moves from the center of the core to the upper third of the core. This was largely due to the fact cold coolant enters at the top of the core. The colder temperatures tends to provide an increased reactivity coefficient. The moderator coefficients follow a similar trend, where the largest feedback coefficients shift from the middle of the fuel region to the upper third of the core. Finally, the reflector coefficients shift form the middle of the reflector region to the upper region. Again, this is expect, as we found both this shift in the fuel and moderator coefficients. Given the lower temperatures in this region, it is expected neutrons which are reflected into the core from the reflector region have a considerably higher probability to cause a fission, hence, the increase in the moderator reactivity coefficient.

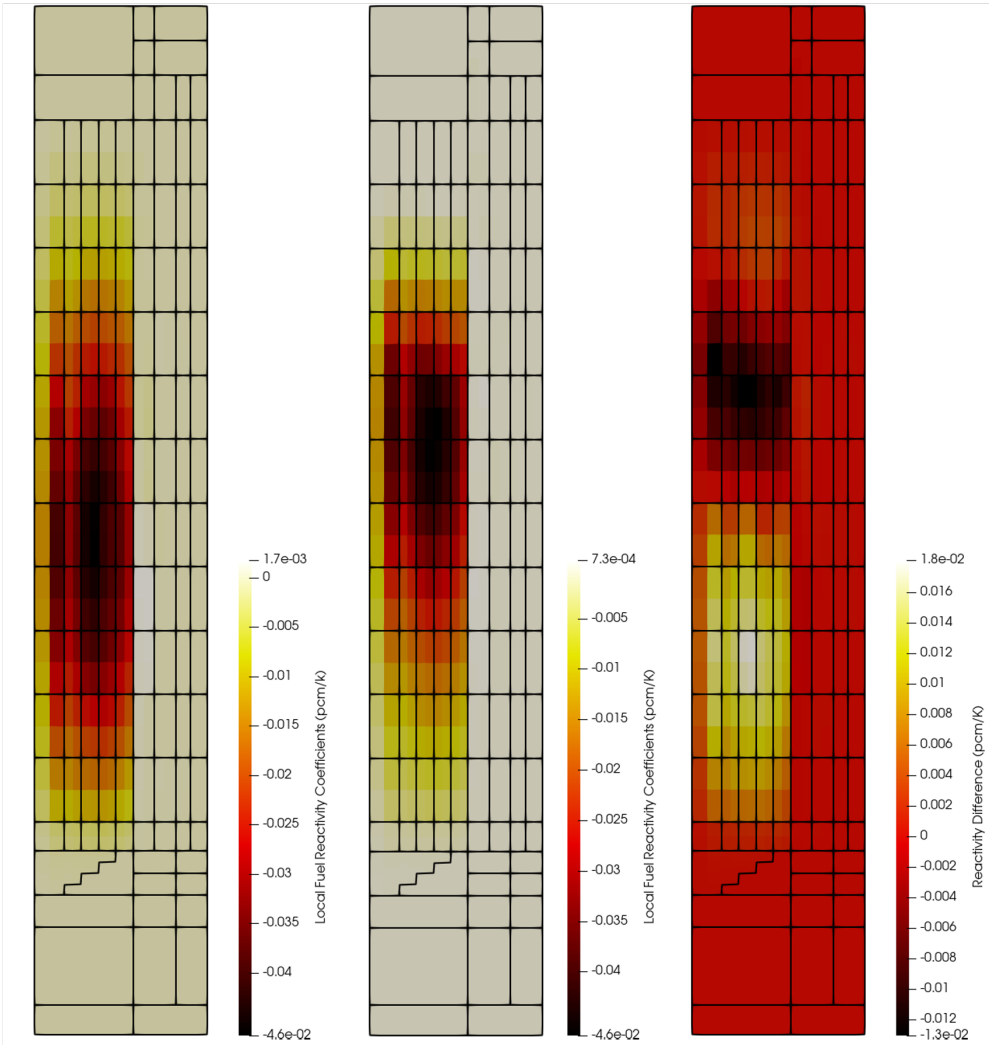

Figure 7: Local fuel reactivity coefficient for each element in the coupled-realistic model. Left: steady state; middle: coupled; right: difference.

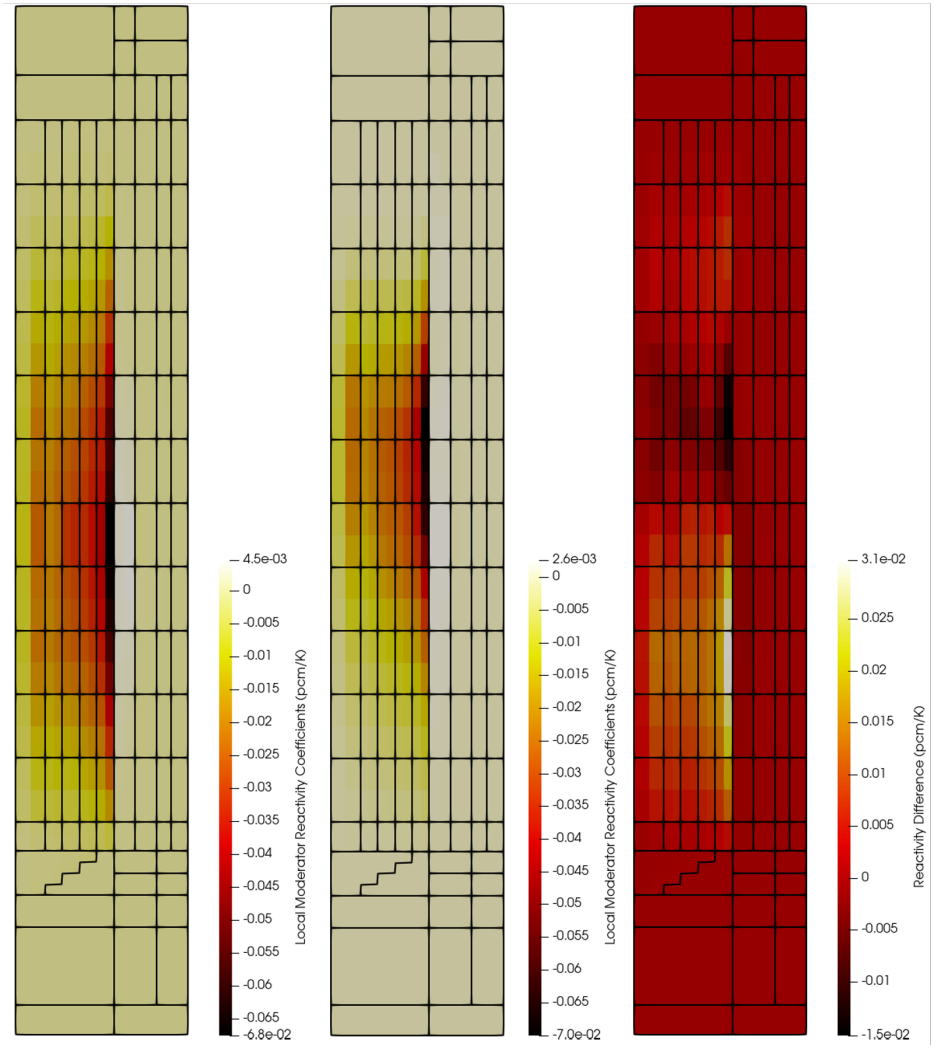

Figure 8: Local moderator reactivity coefficient for each element in the coupled-realistic model. Left: steady state; middle: coupled; right: difference.

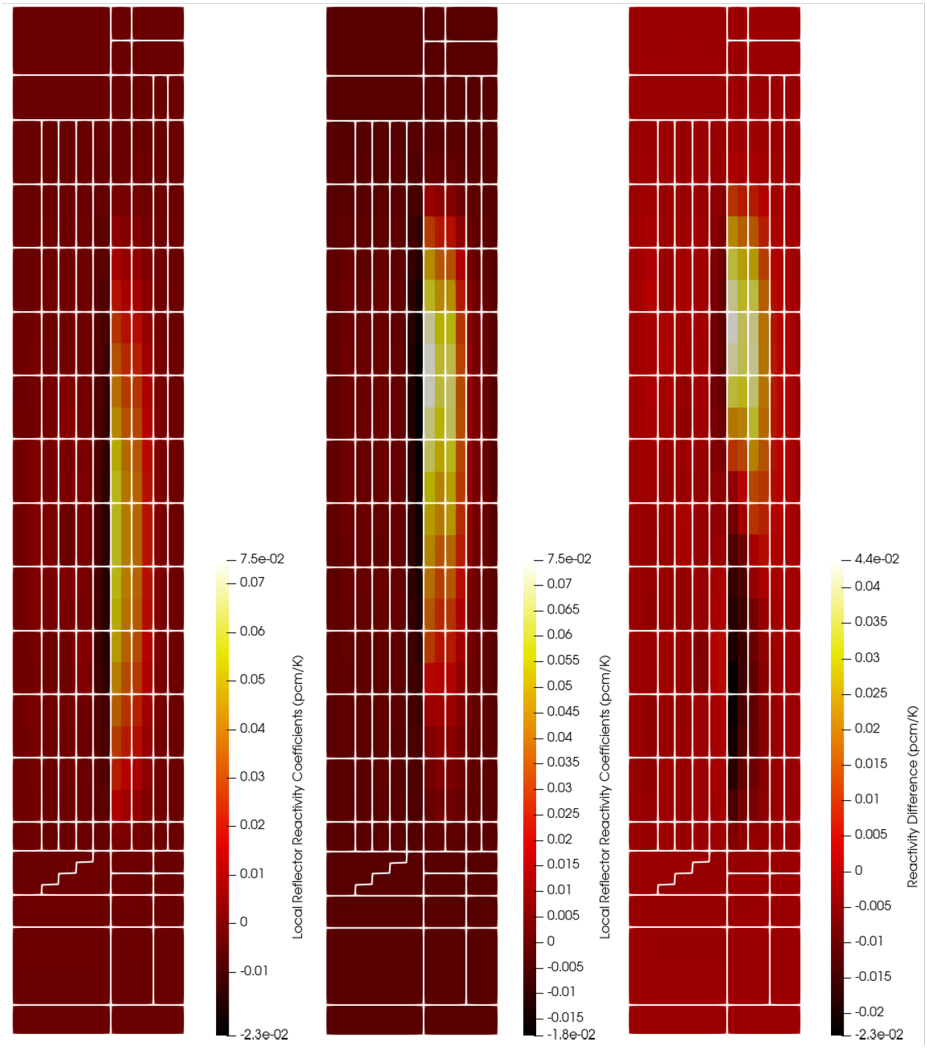

Figure 9: Local reflector reactivity coefficient for each element in the coupled-realistic model. Left: steady state; middle: coupled; right: difference.

3.2 Griffin Standalone Steady-State Results

For the realistic core model, the same process outlined in Section 2.2 was used; only the SPH-corrected cross-section results are presented. The k_{eff} is compared again with Serpent to ensure the SPH-corrected cross sections are accurate The resulting k_{eff} is presented in Table 12, along with the k_{eff} from the temperature profile obtained from Pronghorn. No comparison is made to Serpent as only state points were calculated not specific temperature profiles.

	900 K	Pronghorn Temperature Profile
Serpent	1.32987 (4.3E-05)	–
Griffin	1.32988	1.329423
Diff. (pcm)	1	–

Table 12: Griffin steady state analysis comparison for realistic core model.

Along with k_{eff}, the scalar and adjoint flux for the steady-state solutions are obtained and presented. Figure 10 show both the scalar and adjoint flux distribution in the core. We find the thermal scalar flux shows a slight bimodal distribution with the largest highest fluxes present in the center of the core and in the reflector adjacent to the core. This distribution is due to neutrons being thermalized in the reflector region and reflecting back into the core. The overall distribution of flux coincides well with the flux found in the simplified model (not shown).

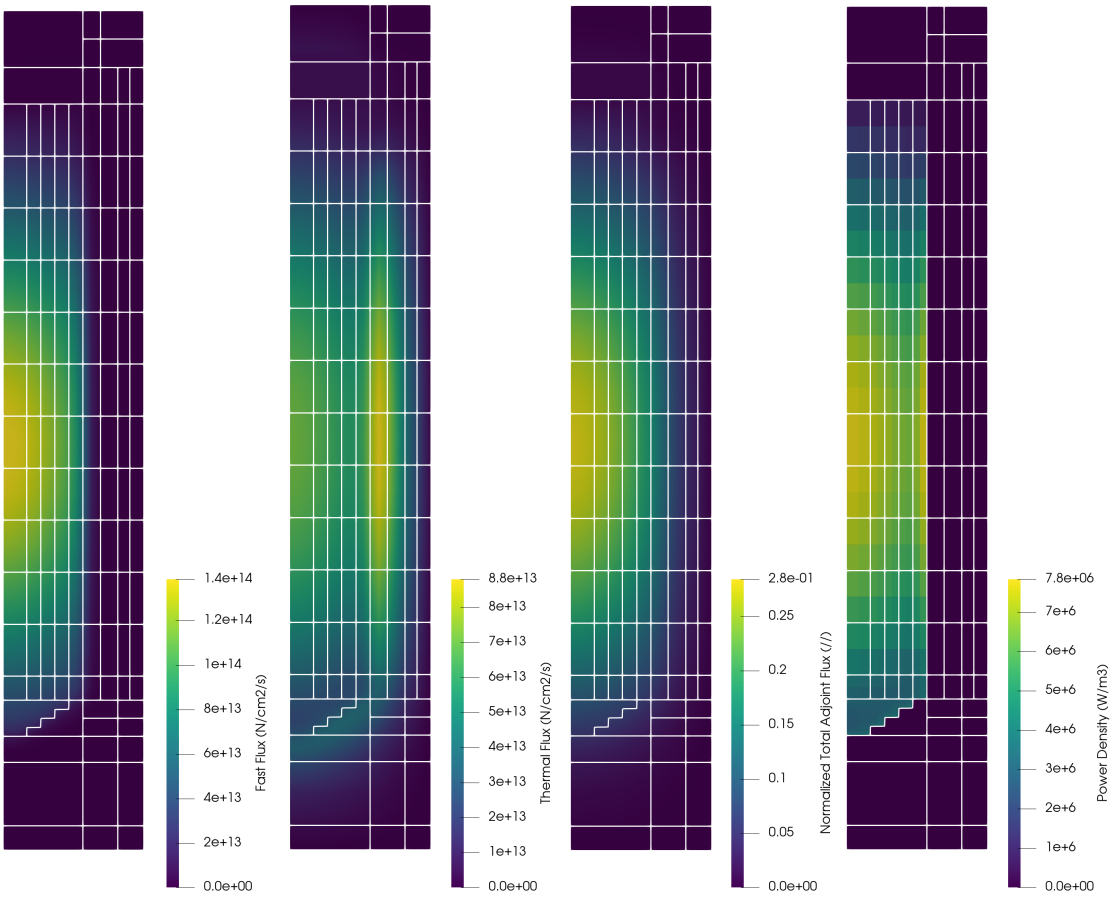

Figure 10: Fluxes and power density calculated from the constant temperature model (900 K).

3.3 Griffin Standalone Reactivity Insertion Transients

Two Griffin standalone reactivity insertion transients (Transient I&II) were used to test the realistic model. For the first transient (Transient I), both the locally and globally generated fuel reactivity coefficients were used. Figure 11 shows the scaled power profile for the reference diffusion solution in addition to the PKE module using both locally and globally produced reactivity coefficients. Along with this, Figure 12 shows the percent difference between the diffusion solution and the locally/globally produced reactivity coefficients. For both locally and globally produced reactivity coefficients, the percent difference from the reference solution was less than 0.1 %.

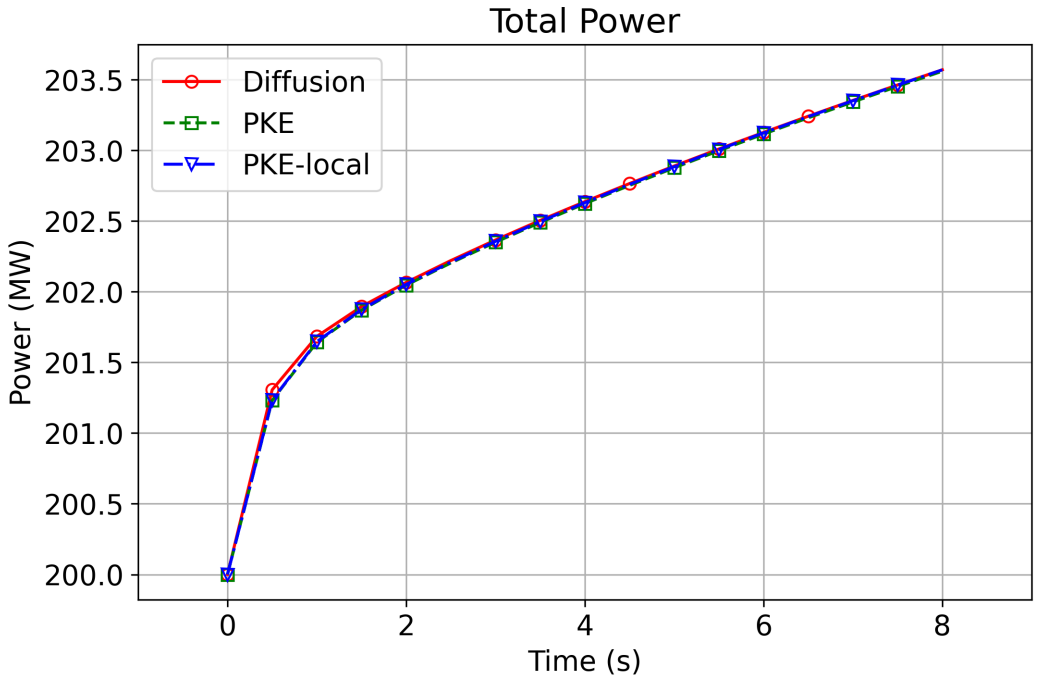

Figure 11: Power profile for locally and globally generated fuel reactivity coefficients for Transient I.

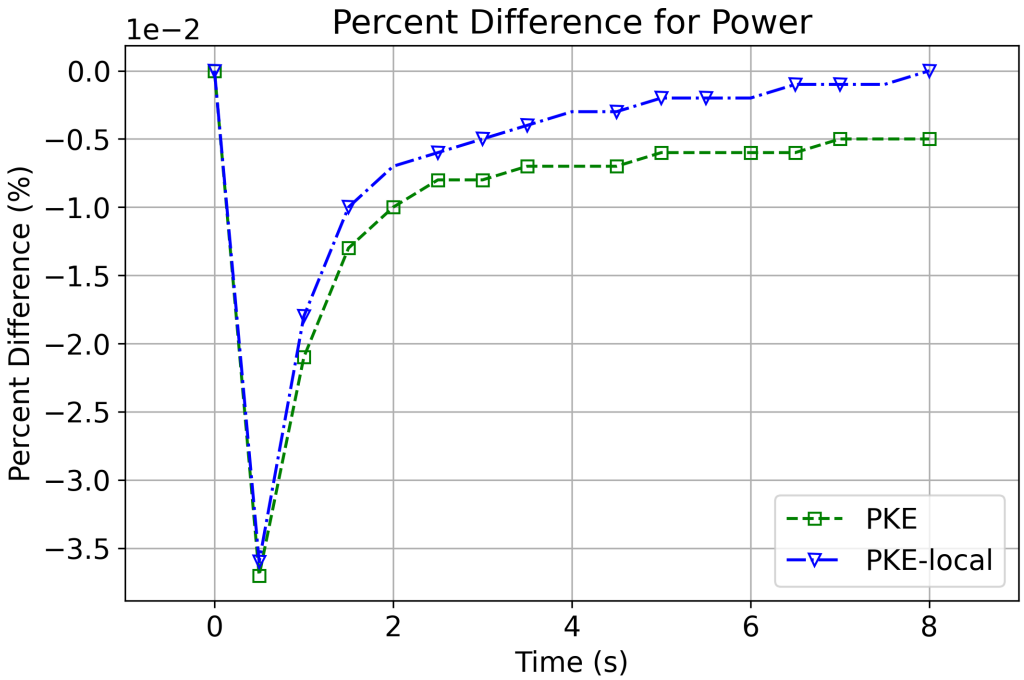

Figure 12: Percent difference for the power for locally and globally generated fuel reactivity coefficients for Transient I.

The next test transient (Transient II) was to examine how globally and locally produced reactivity coefficients can determine a localized transient. To do this, the temperature in the upper half of the core was decreased by 1 K, while the remainder of the core was held at 900 K. Figure 13 shows the locally produced reactivity coefficient was able to match the power profile; however, the globally produced reactivity overestimates the power. Figure 14 shows the percent difference for locally and globally produced reactivity coefficients when compared with the diffusion solution. While the difference for a 1 K temperature change was within 1%, greater differences may occur for larger transients.

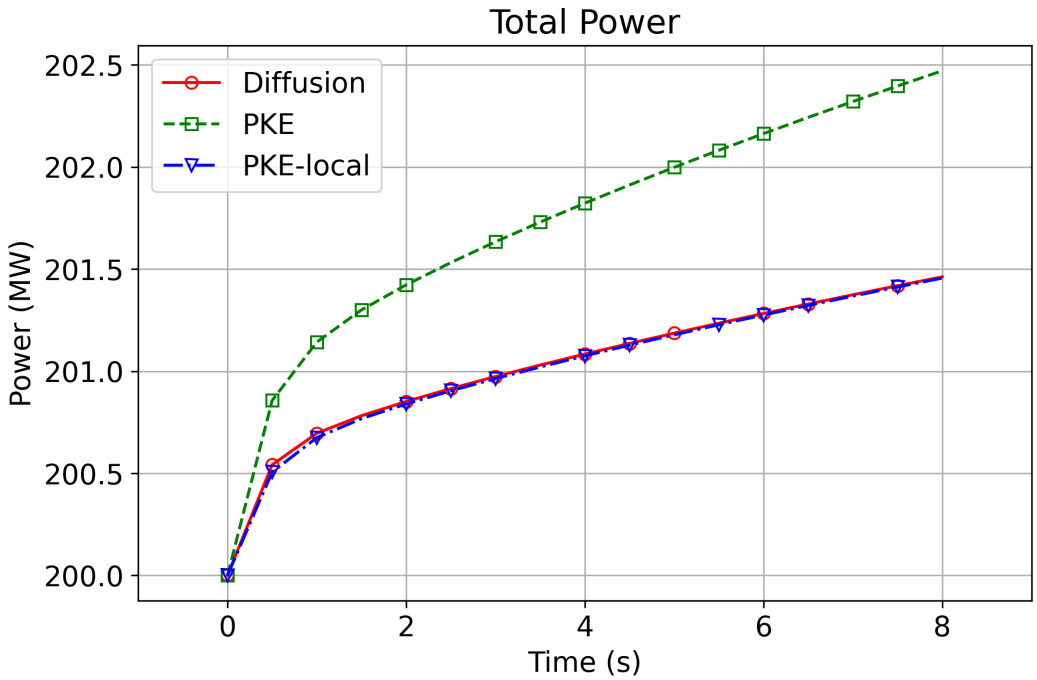

Figure 13: Power profile for locally and globally generated fuel reactivity coefficients for Transient II.

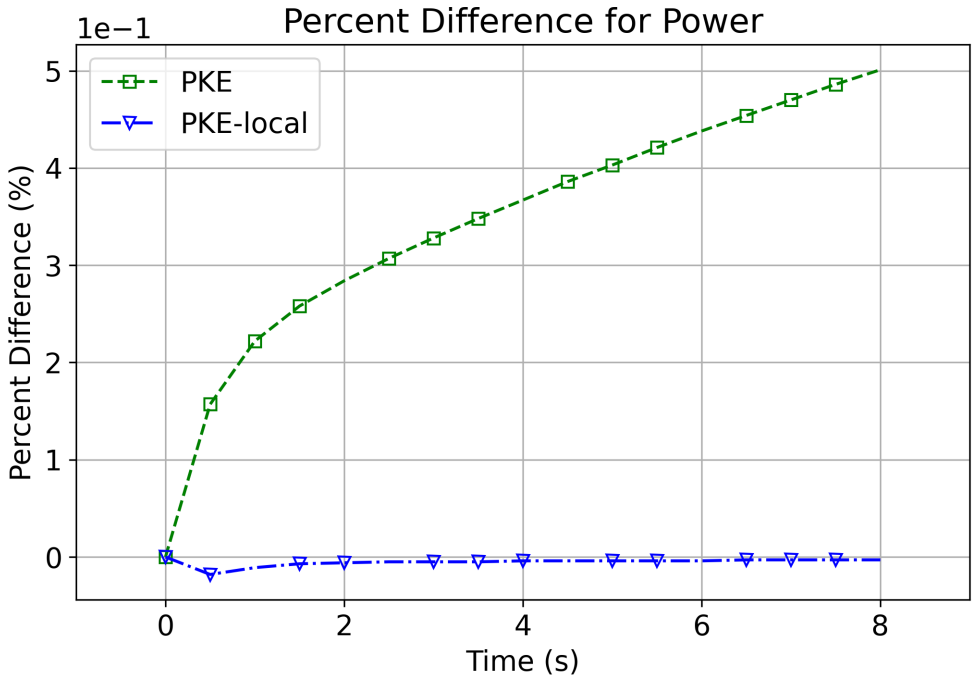

Figure 14: Percent difference for the power for locally and globally generated fuel reactivity coefficients for Transient II.

3.4 Coupled Steady State Results

After establishing the two independent models, the NK and TH models were coupled together for steady state and transient analysis with Griffin serving as the master application. The power density is calculated in Griffin and passed to the Pronghorn model. The Pronghorn model then calculates the fuel, moderator, and reflector temperatures and pass them back to the Griffin to interpolate cross sections and update power profile. The resulting pressure, fuel, moderator, and reflector temperatures may be found in Figure 15. The velocity streamlines are also seen over the pressure field. It can be seen the fluid follows the expected flow path, entering on the right side of the core inlet, proceeding up through the riser and across the top void, then down through the bed and out through the right of the outlet plenum. Given the prescribed outlet pressure of 5.84 MPa, the inlet pressure is calculated to be 5.98 MPa compared to the 6 MPa literature value. This model with the literature mass flow rate of 78.6 kg/s and inlet temperature of 533 K produces a core outlet temperature of 1024 K, compared to the expected literature value of 1023 K. These results demonstrate good agreement with the expected parameters. The NK results can be found pictured in Figure 16. The flux and power peaks are on the top half of the core despite the inserted control rods due to the strong temperature gradient from top to the bottom of the reactor that increases the non-fissile capture events in the bottom half. The power profile has a shape to similar to the thermal flux as expected since the most of the fission event happen in the thermal range. The thermal flux and power profile show a radial peak close to the reflector because a considerable amount of neutrons that escape the bed are thermalized and scattered back into the pebble bed. The adjoint flux that will be used for the IQS module is higher toward the center of the pebble bed as expected since this is where most of the neutron that induce fission are born.

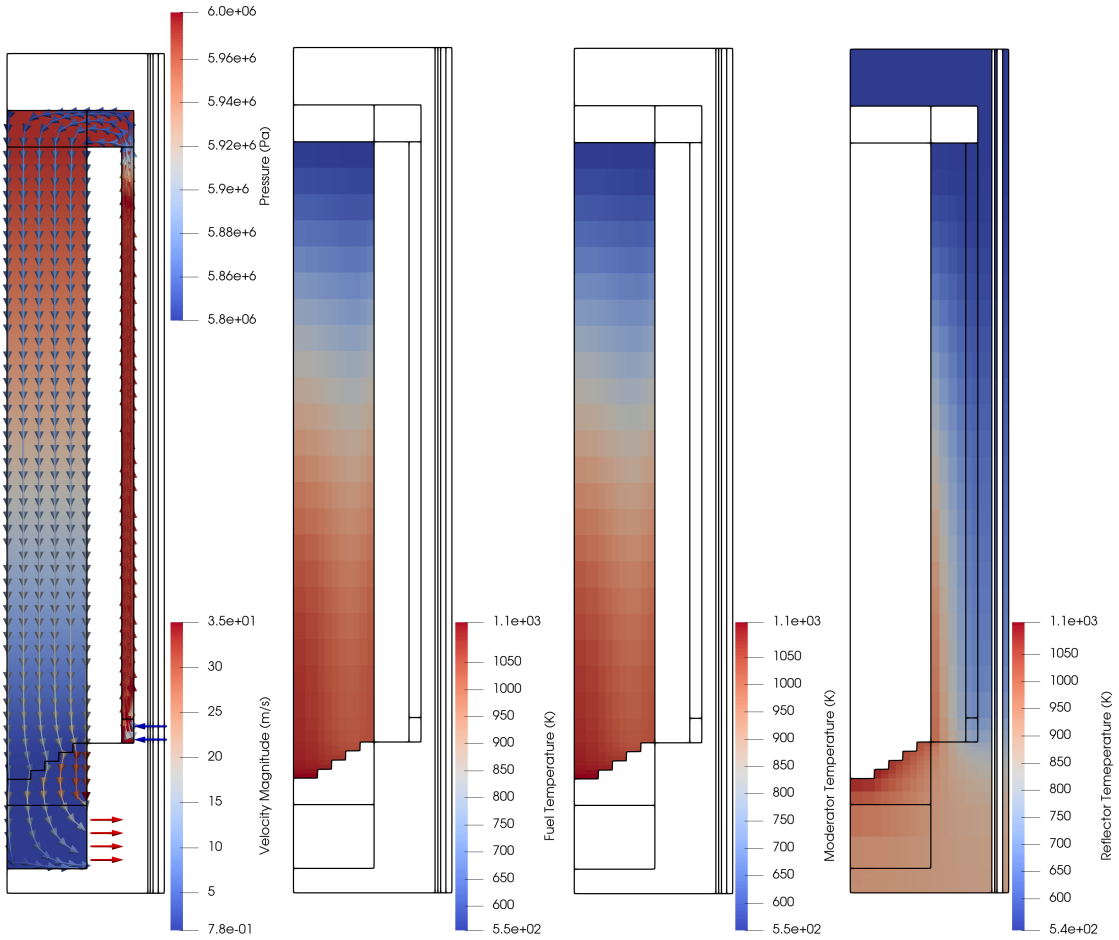

Figure 15: Pressure, fluid temperature, and solid temperatures calculated using the steady-state coupled model.

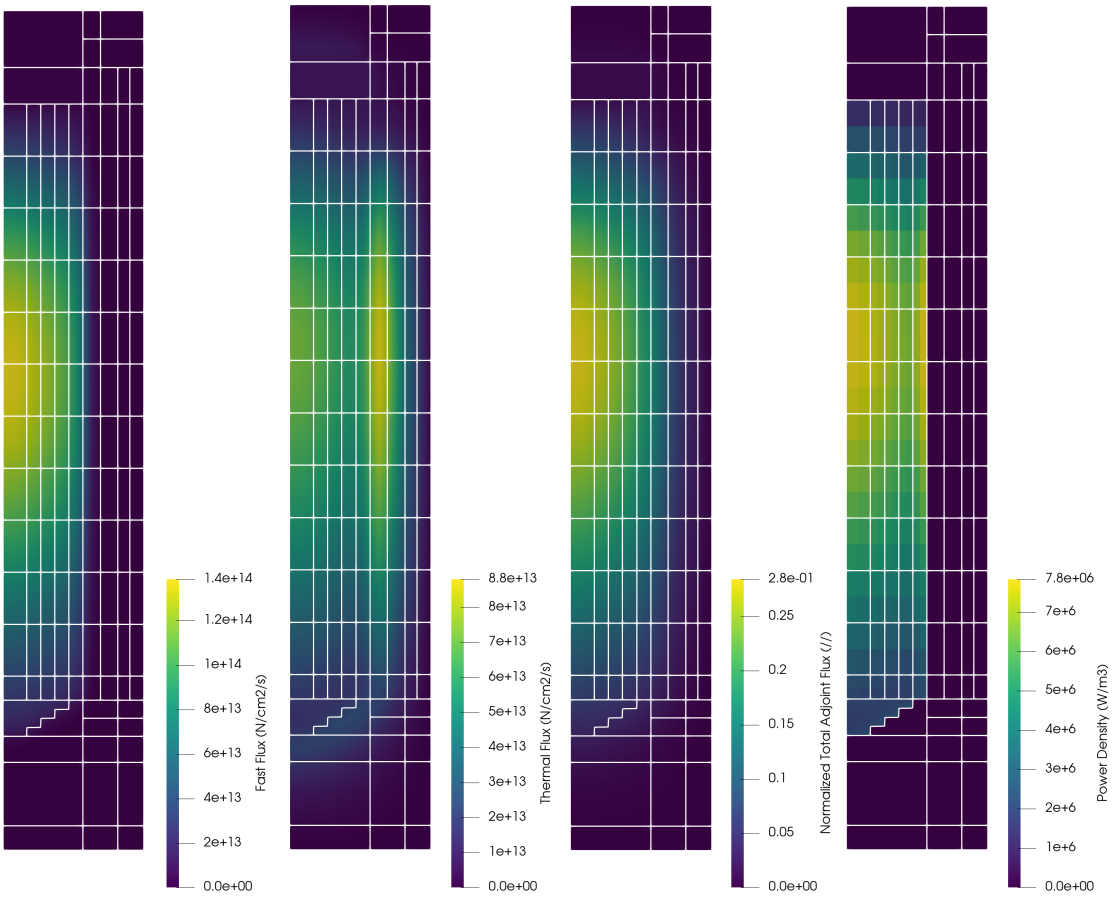

Figure 16: Fluxes and power density calculated using the steady-state coupled model.

3.5 Coupled Load-Following Transient

A coupled transient case was setup in order to test the load-following capabilities of the system. This transient was performed with the diffusion scheme, the PKE scheme, and the local reactivity coefficient PKE scheme to evaluate how well the lower fidelity schemes (PKE and PKE local) were able to match the results of the higher fidelity model (diffusion) in a realistic situation. This was done by ramping the mass flow rate into the core in the TH model from 100% to 25% over the course of 15 minutes. After 45 minutes, the mass flow rate was then ramped back up from 25% to 100% over 15 minutes and the system was allowed to stabilize. The timing of this ramp was chosen to achieve the 5% per minute load-following requirement described in [15]. The same time step and TH pronghorn input file was used for the different methodologies to avoid the introduction of numerical error. As shown in Figures 17 and 18, the total reactor power decreases roughly linearly along with the mass flow rate, as expected. At the start and end points of the ramps, there are some small oscillations as a result of delayed neutrons and delayed thermal hydraulic feedback. The power changes similarly between the diffusion the different models with the PKE model and the PKE model with local coefficients, predicting roughly 3% and 0.1% lower power than the diffusion model respectively. In general, the predicted temperatures follow an opposite trend compared to the results found in [15] because no RCS is used to control the outlet helium temperature and as shown in Figure 19 is free to change based on the total power mass flow rate conditions. Despite the small discrepancy in the total power prediction, the fuel, moderator, and reflector temperatures show a significant discrepancy between the coupled diffusion model and the two PKE and PKE with local coefficients models as shown in Figures 20, 21, and 22. Using local coefficients to reduce the error of the results introduced almost no increase in the computational time. This can be extremely important especially for the fuel temperature, as exemplified in Figure 20, where using global reactivity coefficients completely inverts the trend of the transient.

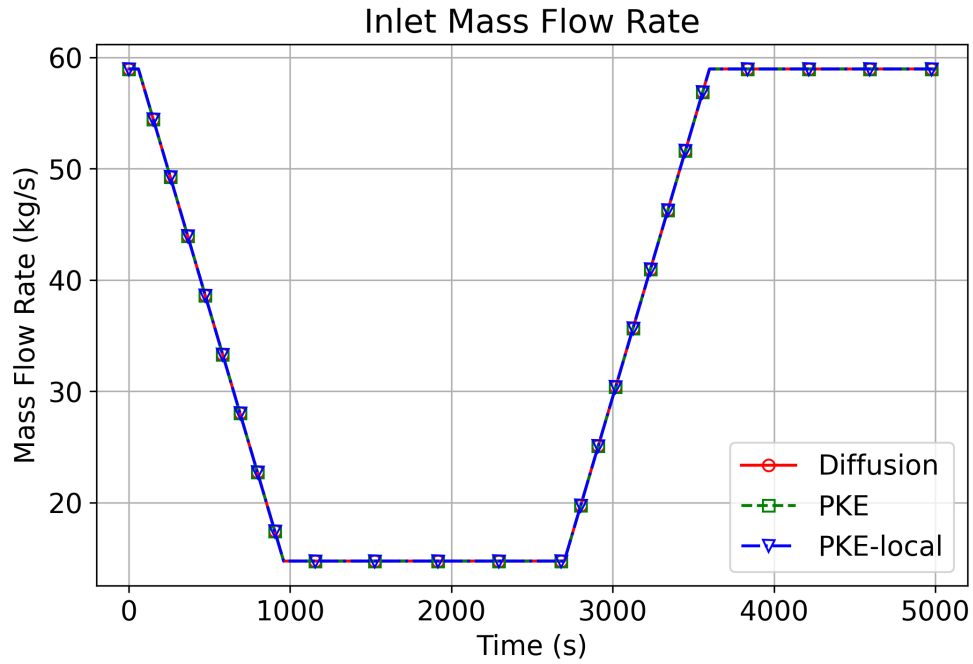

Figure 17: Inlet mass flow rate during the load-following transient.

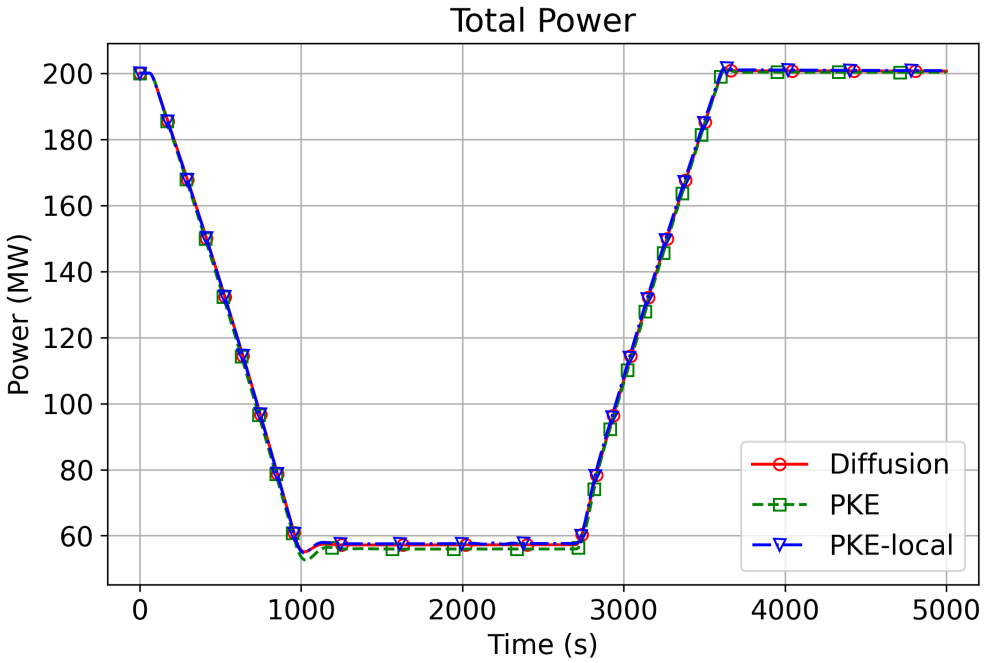

Figure 18: Total reactor power during the load-following transient.

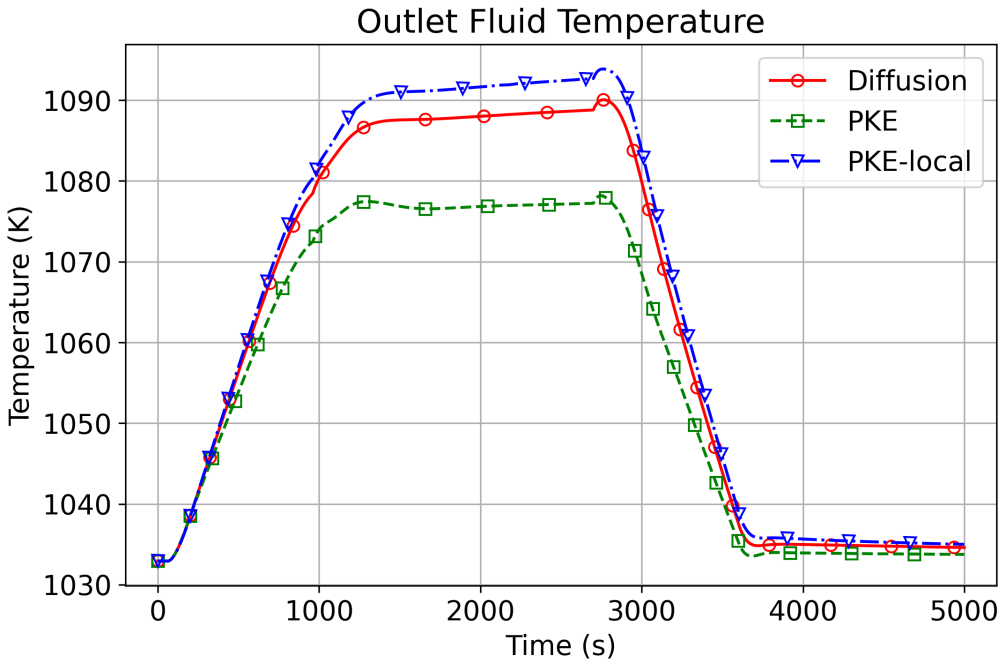

Figure 19: Outlet fluid temperature during the load-following transient.

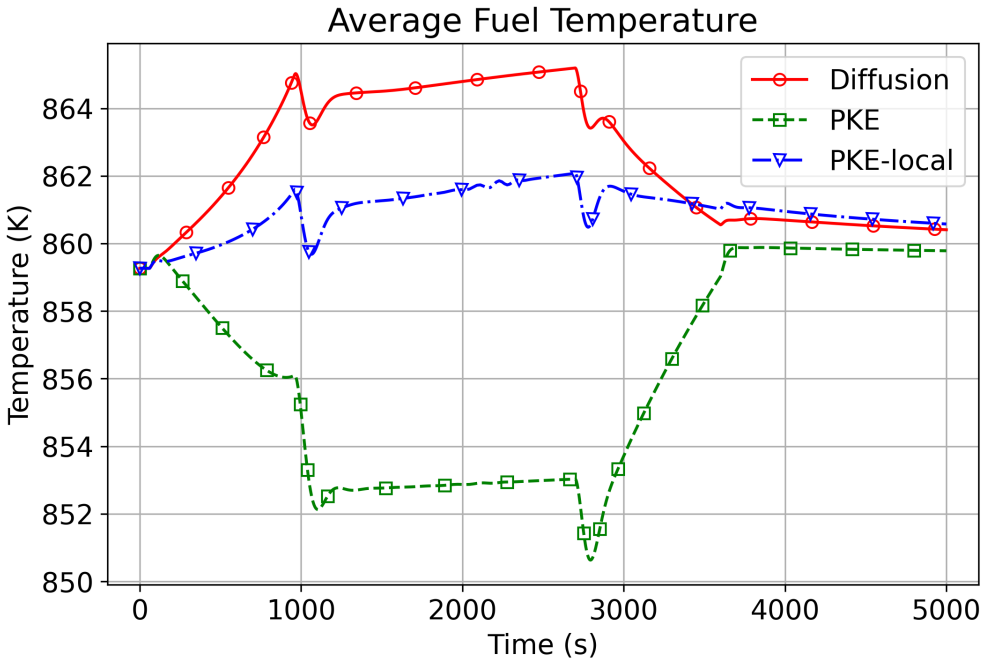

Figure 20: Average fuel temperature during the load-following transient.

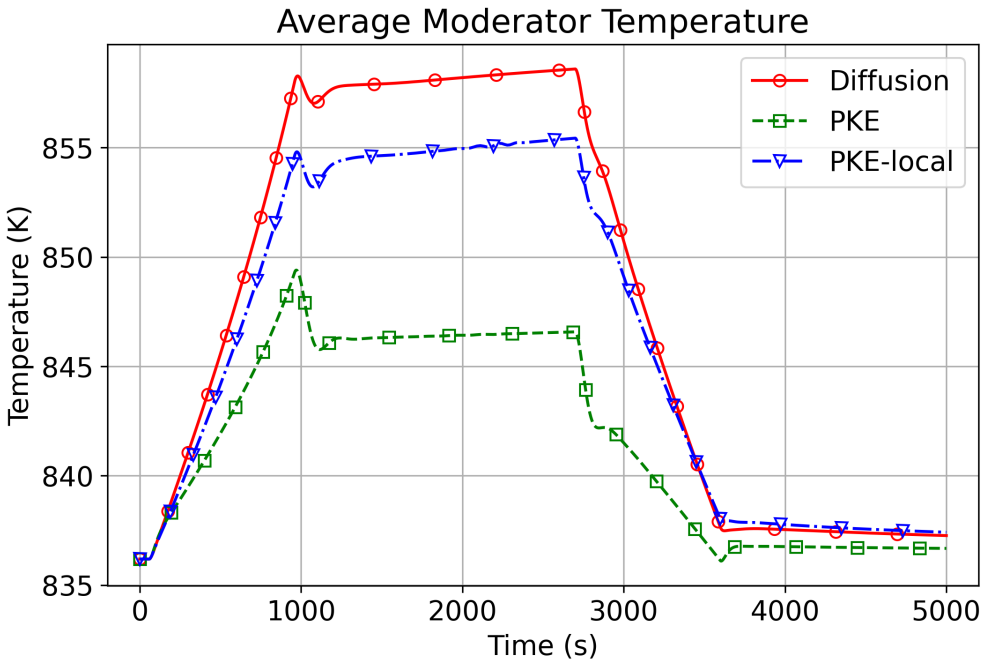

Figure 21: Average moderator temperature during the load-following transient.

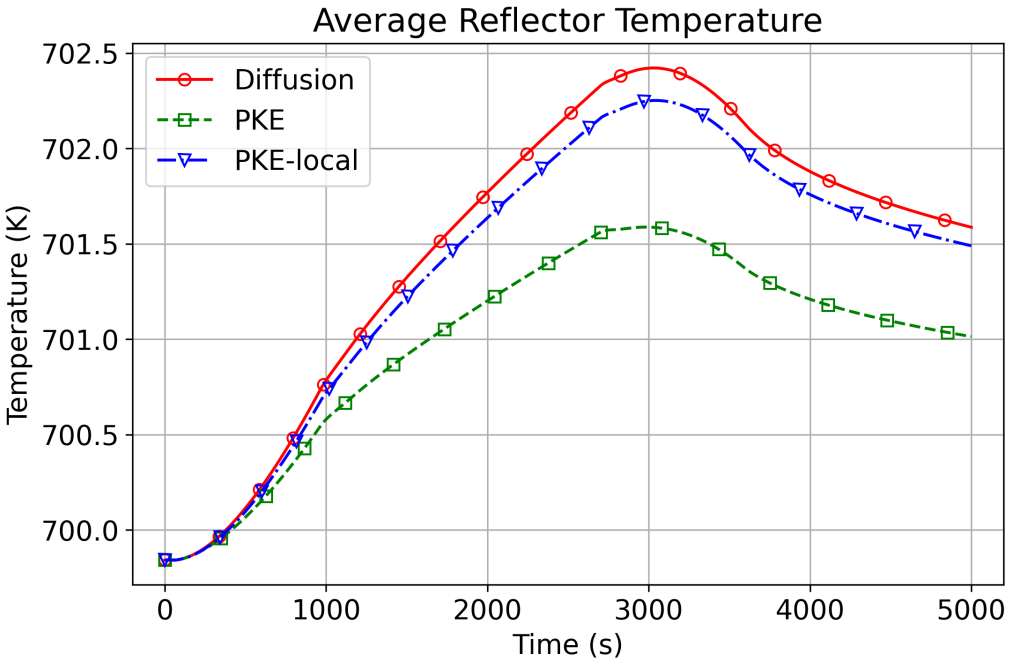

Figure 22: Average reflector temperature during the load- following transient.

The discrepancies on the different temperatures translate to differences in the calculated reactivities as shown in Figures 23–26. The fuel temperature calculated reactivities in Figure 23 are very similar to the moderator, where the reflector temperature are quite different as shown in Figures 24 and 25. It is likely that the moderator and reflector temperature errors compensate each other since the total calculated reactivity is in good agreement as shown in Figure 26.

A comparison between partial and total reactivities for both the PKE and PKE with local coefficients schemes are shown in Figures 27 and 28. We find the temperature of the reflector and the moderator increase faster on the PKE with local coefficients introducing respectively more positive and negative reactivity because of the higher predicted power (closer to the higher fidelity diffusion calculation). The fuel temperature is very sensitive to the graphite matrix temperature (imposed as a BC at the outer surface of the representative TRISO particle) and strongly depends on the power level since positive insertion of reactivity from the fuel temperature is due to the reduction in power that immediately shows in the TRISO particle.

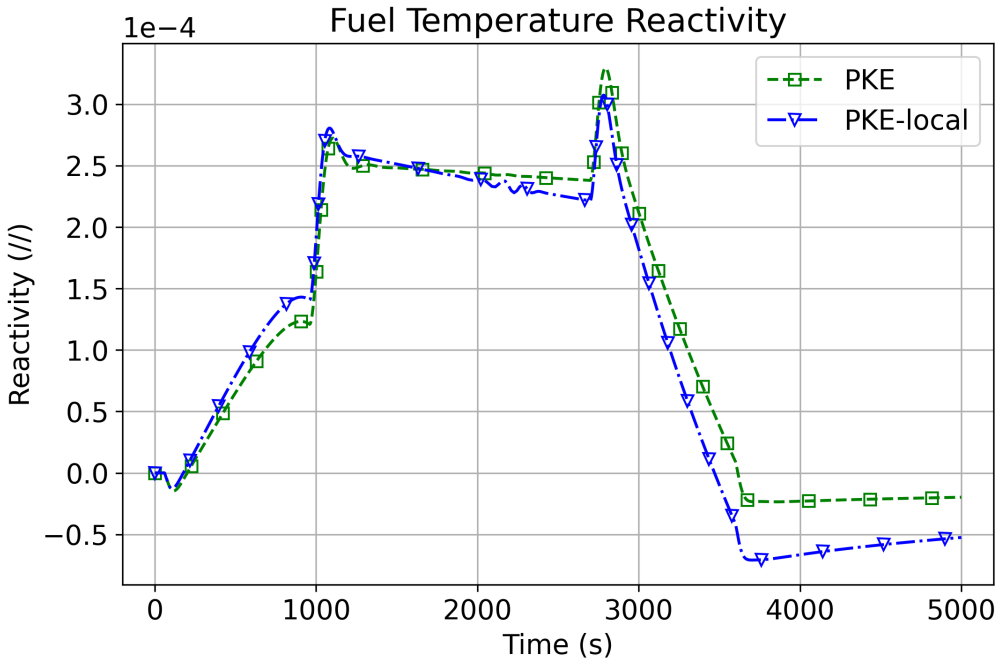

Figure 23: Reactivity inserted by the fuel temperature change during the load-following transient.

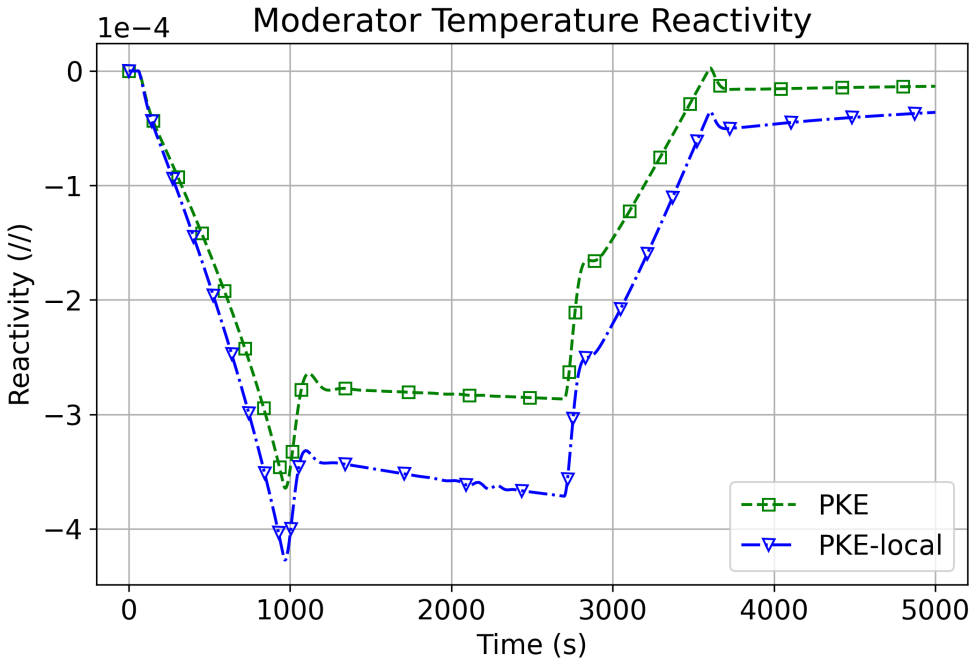

Figure 24: Reactivity inserted by the moderator temperature change during the load-following transient.

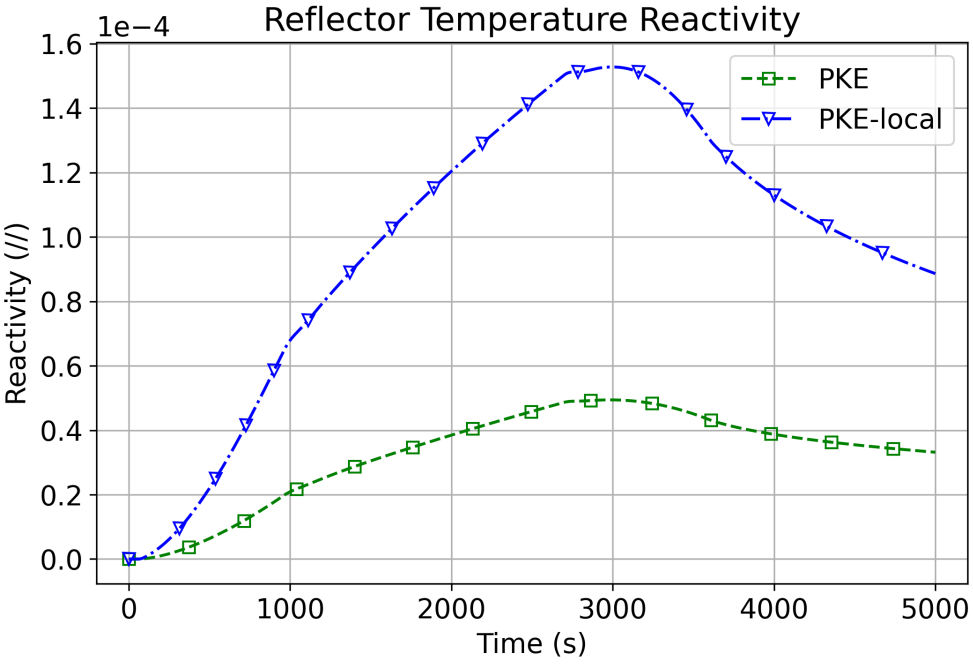

Figure 25: Reactivity inserted by the reflector temperature change during the load-following transient.

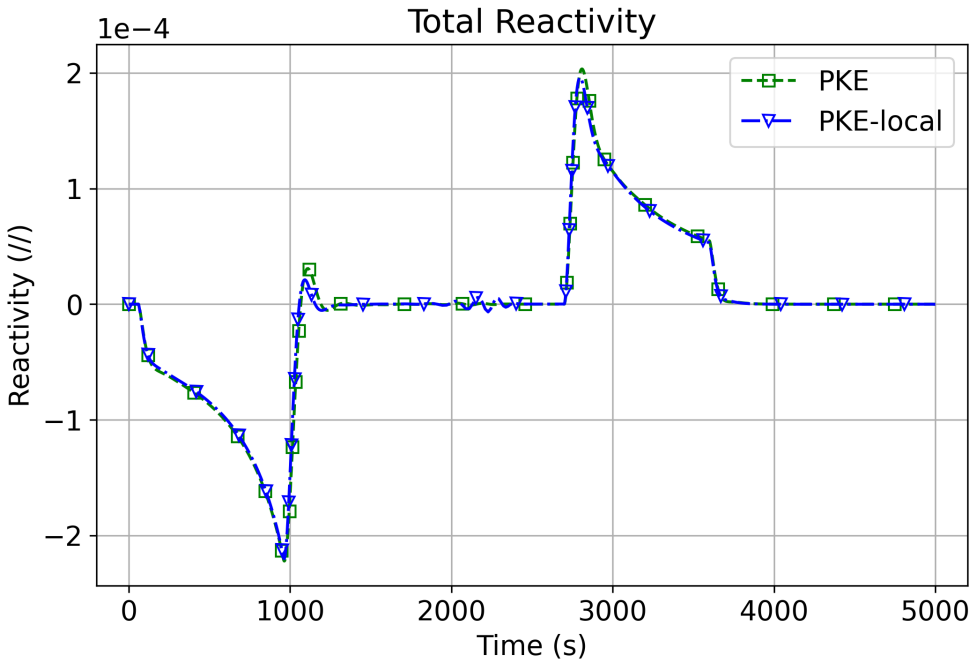

Figure 26: Total reactivity during the load-following transient.

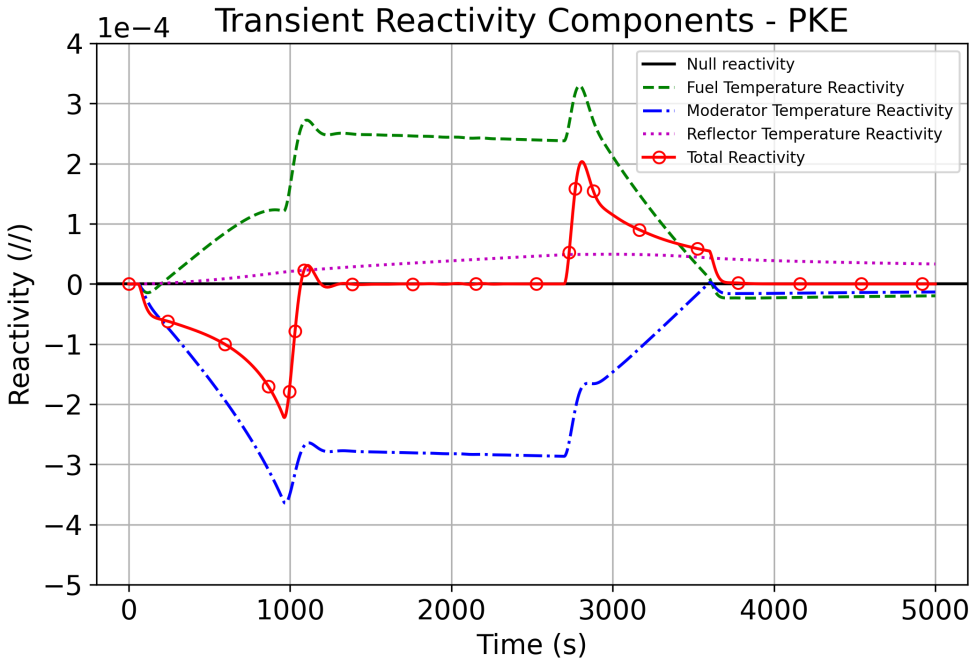

Figure 27: Partial and total reactivities during the load-following transient using the PKE scheme.

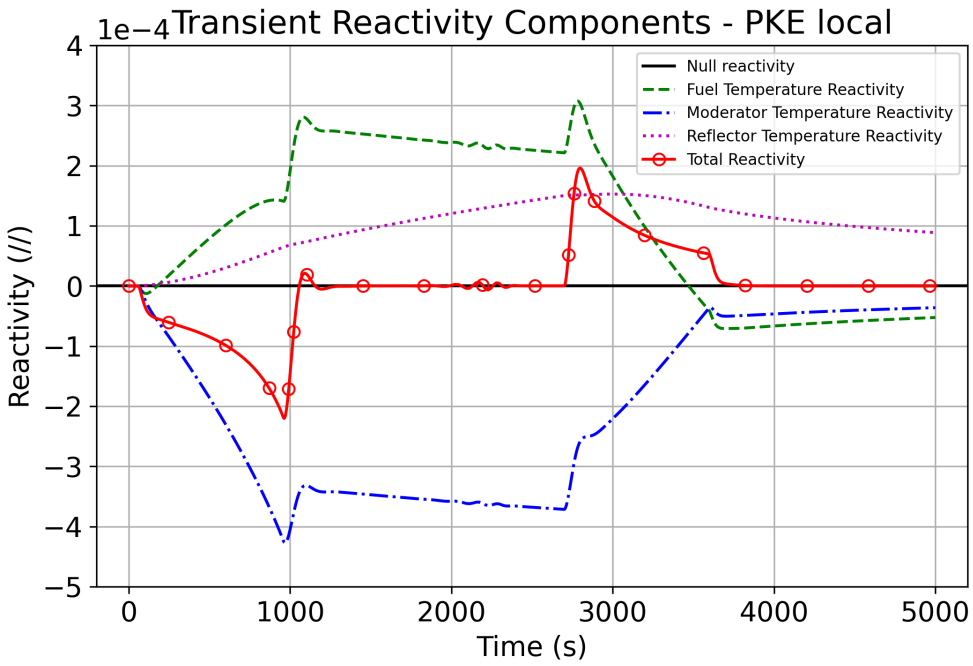

Figure 28: Partial and total reactivities during the load-following transient using the PKE scheme with local coefficients.

4. CONCLUSIONS AND FUTURE WORK

Griffin and Pronghorn were selected as a tool set for studying HTGRs behaviour during accident scenarios based on the ongoing and previous experience in modeling this type of reactors. Given a cross-section set, Griffin was able to generate reactor point kinetics parameters and reactivity coefficients (both global and local coefficients) that are essential for fast running calculations of $\sim$100h long design basis accidents and or anticipate operating occurrences that can be used for design optimization studies or dynamic probabilistic risk assessment. The current study demonstrated how the PBR performances can be predicted accurately in the limit of the PKE models (constant power shape). The usage of the local reactivity coefficients reduced the maximum error on the total power from 5% to below 1.5%, and the porous media temperatures (fluid, fuel, moderator, and reflector) error from 12 K to below 4 K with negligible additional computational time; hence, the use of local coefficients for fast transient calculations is recommended. The research activities demonstrated how the coupled NEAMS tools can accurately calculate PKE parameters and temperature coefficients leveraging the existing code capabilities. The next steps will focus on two areas: first, the calculation of reactivity coefficients for Xenon and the generation of reactivity tables for the RCS; and second, replacement of fresh fuel compositions with equilibrium core composition (capability under development in the NEAMS tools) to make sure the reactivity coefficients are representative of a real core configuration.

REFERENCES

[1] E. J. Mulder and W. A. Boyes, "Neutronics characteristics of a 165 mwth xe-100 reactor," *Nuclear Engineering and Design*, vol. 357, p. 110415, 2020.

[2] M. A. Pope, "Transmutation analysis of enriched uranium and deep burn high temperature reactors," Tech. Rep. INL/EXT-12-26423, Idaho National Laboratory, July 2012.

[3] C. Permann, D. Gaston, D. Andrs, R. Carlsen, F. Kong, A. Lindsay, J. Miller, J. Peterson, A. Slaughter, R. Stogner, and R. Martineau, "Moose: Enabling massively parallel multiphysics simulation," *Preprint submitted to SoftwareX*, 2020.

[4] Y. Wang, S. Schunert, and V. Laboure, *Rattlesnake Theory Manual*. Idaho National Laboratory, 2017.

[5] E. R. Shemon, M. A. Smith, and C. H. Lee, "Proteus-sn methodology manual," tech. rep., Argonne National Laboratory, 2014.

[6] C. Lee and W. S. Yang, "Mc2-3: Multigroup cross section generation code for fast reactor analysis," *Nuclear Science and Engineering*, vol. 187, no. 3, pp. 268–290, 2017.

[7] Y. Wang and et al., "Rattlesnake: A moose-based multiphysics multi-scheme radiation transport application," *submitted to Nuclear Technology*, 2020.

[8] J. Leppänen, M. Pusa, T. Viitanen, V. Valtavirta, and T. Kaltiaisenaho, "The serpent monte carlo code: Status, development and applications in 2013," *Annals of Nuclear Energy*, vol. 82, pp. 142–150, 2015.

[9] Y. Wang and J. Ortensi, *YAKXS - The XML Multigroup Cross Section Library*. Idaho National Laboratory.

[10] A. Novak, R. Carlsen, S. Schunert, P. Balestra, R. Slaybaugh, and R. Martineau, "Pronghorn: A multidimensional coarse mesh application for advanced reactor thermal-hydraulics," *Nucl. Tech.*, vol. submitted, 2020.

[11] A. Novak, S. Schunert, R. Carlsen, P. Balestra, R. Slaybaugh, and R. Martineau, "Multiscale thermal-hydraulic methods for salt-cooled pebble bed reactors," *Annals of Nuclear Energy*, vol. submitted, 2020.

[12] P. Balestra, S. Schunert, R. W. Carlsen, A. J. Novak, M. D. DeHart, and R. C. Martineau, "Pbmr-400 benchmark solution of exercise 1 and 2 using the moose based applications: Mammoth, pronghorn," in *Proceedings of PHYSOR 2020: Transition to a Scalable Nuclear Future*, (Cambridge, United Kingdom), March 29th-April 2nd 2020.

[13] J. W. Peterson, A. D. Lindsay, and F. Kong, "Overview of the incompressible navier–stokes simulation capabilities in the moose framework," *Advances in Engineering Software*, vol. 119, pp. 68 – 92, 2018.

[14] Suwoto, H. Adrial, Kuhair, K. Kamajaya, and S. Bakhri, "Analysis of heavy metal loading optimization through criticality calculation on rde," in *Journal of Physics: Conference Series*, vol. 1198, p. 022004, IOP Publishing, 2019.

[15] Y. Brits, F. Botha, H. van Antwerpen, and H. W. Chi, "A control approach investigation of the xe-100 plant to perform loadfollowing within the operational range of 100–25–100%," *Nuclear Engineering and Design*, vol. 329, pp. 12–19, 2018.

Appendix A
Determination of Mean Generation Time

From Section 2.2.3, we found the mean generation time between Griffin and Serpent did not agree. To quantify the effect of the mean generation time, we examine a 5 K transient . Using the PKE module, we compare the results using the mean generation time from Serpent and the Griffin. The transient and percent difference compared with the diffusion solve can be seen in Figure 29 and Figure 30. By the end of the 10 second transient, we find the solution differs by less than 0.5%. While there is a noticeable difference, results using the mean generation time from Griffin are expected to be relatively accurate. Further investigation is ongoing to determine the cause of the difference in the mean generation time.

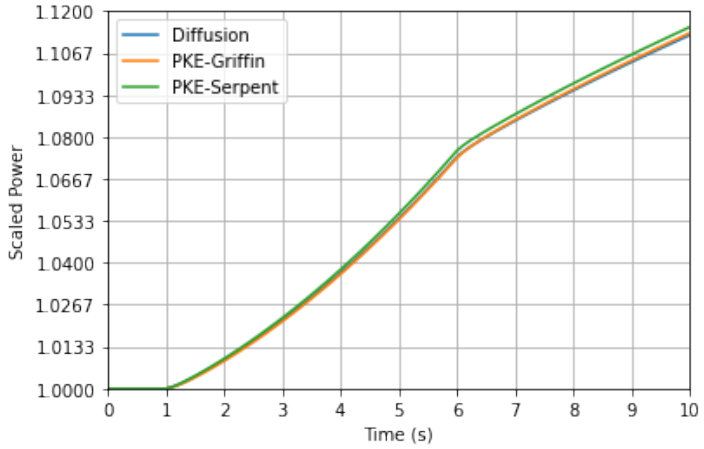

Figure 29: Temperature Transient I for comparing Serpent and Griffin mean generation time.

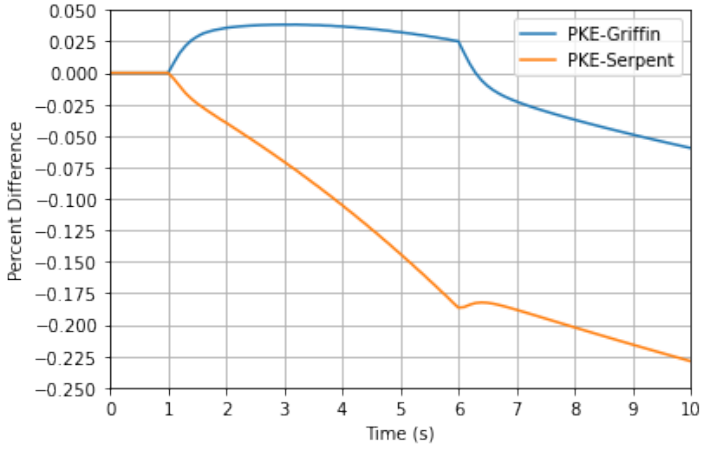

Figure 30: Percent difference in power for for comparing Serpent and Griffin mean generation time.